Shape, oscillation modes, and orientation dynamics of aerodynamically levitated nanofluid drops

Gene Patrick S. Rible,[1] Syed Jaffar Raza,[1] Connor K. Traynor,[1] Joshua T. Watkins,[1] Hannah P. Sebek,[1] Alexander R. Bottoms,[1] Tadd T. Truscott,[2] and Andrew K. Dickerson[1,*]

[1]*Department of Mechanical, Aerospace and Biomedical Engineering, University of Tennessee, Knoxville, Tennessee 37996, USA*

[2]*Physical Science and Engineering Division, King Abdullah University of Science and Technology, Thuwal, Saudi Arabia*

(Received 30 October 2025; accepted 22 April 2026; published 15 May 2026)

In this experimental study, we introduce methods to characterize drop oscillation and shape using a two-camera setup inspired by two-dimensional video disdrometers. The two cameras maintain close proximity to the levitating drop, enabling high-fidelity three-dimensional reconstruction of drop orientation and dynamics. The prevailing drop shadow in each camera view is extracted to determine a time-averaged characteristic shape, from which a volume-equivalent characteristic diameter D_0 is obtained via disk integration. We find strong agreement between our measured D_0 and established models of axis ratio and equilibrium drop shape. A frequency analysis along the drop shadow perimeter reveals the presence of three dominant modes, i.e., axisymmetric (2, 0), horizontal (2, 2), and transverse (2, 1), with the axisymmetric mode the most prominent and resilient to noise. We define a nondimensional total oscillation amplitude which enables comparison of oscillation intensities across drop conditions. The addition of nanoparticles increases interfacial tension and, at low concentrations (<0.5% m/m), promotes deformation through heterogeneous distributions and interfacial instabilities. These effects enhance canting amplitude, canting angular velocity, and results in an unsteady orientation, sometimes leading to a full circulation of the drop. Beyond a nanoparticle saturation concentration (NSC) of approximately 0.5% m/m, surface-bound nanoparticles stabilize the drop, reducing canting and total oscillation amplitude. The presence of surfactant increases the NSC by capturing surface particles into micelles, delaying interfacial saturation. These findings offer different tools and insights for characterizing complex oscillation dynamics in levitated multiphase drops, with implications for raindrop physics and fluid-interface studies. Our work is an experimental validation of all the accumulated theoretical work on raindrop studies since 1879.

DOI: 10.1103/s7rj-swb3

I. INTRODUCTION

Observing hydrometeor behavior allows researchers to investigate the mechanisms behind cloud condensation [1], aerosol capture [2], and precipitation formation [3,4], which are essential for accurate weather forecasting [5,6]. Instruments such as radar [7–9] and satellite [10] sensors rely on precise measurements of hydrometeor properties such as size, shape, and state to detect the type and determine the intensity of precipitation using empirical models [11–13]. Hydrometeors are rarely pure, often containing aerosol impurities such as hydrocarbons [14], industrial surfactants [15],

*Contact author: dickerson@utk.edu

and biological agents [16]. Impurities enter raindrops during in-cloud nucleation and below-cloud scavenging.

Because impurities strongly influence hydrometeor microphysics and cloud-precipitation dynamics, it is critical to understand the mechanisms through which aerosols are incorporated into raindrops. Atmospheric aerosols of diameter >50 nm can undergo in-cloud scavenging (ICS) by acting as cloud condensation nuclei (CCN) [1,17]. Smaller particles do not typically participate in ICS and amalgamate to form larger particles before acting as CCN [18,19]. Below-cloud scavenging (BCS) is the process of aerosol uptake by falling raindrops, typically driven by Brownian diffusion, impaction, and interception [17,20–23]. Particles experiencing BCS range broadly in size (10–2500 nm), making BCS especially important in the capture of finer nanoparticles. Aerosols can be water soluble or insoluble [24,25]. Certain water-soluble species such as ionic salts increase the surface tension of the solution [26,27]. Insoluble aerosols range from sand to carbon to heavy metals. However, the effects of insoluble particles on raindrop behavior once incorporated remain largely unknown. To address this gap, we use silicon dioxide, a common atmospheric aerosol [28], as a representative insoluble particle to examine its influence on raindrop microphysics.

Soluble species can take the form of various salts and surfactants, lowering surface tension. Sea spray is a primary source for aerosolized salt, while surfactants [29] originate from industrial byproducts, fossil fuel emissions [30], and natural secretion by aquatic plants [31,32]. Surfactants contain both a hydrophobic and hydrophilic component and can be cationic, anionic, or non-ionic [33]. Surfactants typically act at the fluid interface [34], decreasing cohesive forces between molecules and thereby reducing surface tension. At sufficiently high concentration, surfactants interfere with nanoparticles in the fluid medium, forming micelles [35].

Falling raindrops are subjected to the force of gravity, internal circulation, and aerodynamic drag. The drag force on a raindrop F_d is proportional to a coefficient of drag C_d: $F_d = 0.5\rho_a V^2 A C_d$, where ρ_a is air density, V is terminal velocity, and A is the cross-sectional area in contact with the direction of airflow [36]. For distilled water drops less than 1 mm in diameter, the C_d of a raindrop can be approximated to that of a rigid sphere [5,37]. At diameters >1 mm, C_d typically increases beyond that of rigid spheres due to the flattening of the fluid under the influence of aerodynamic drag [5,6]. Further retention or deviation of spherical drop shape can be attributed to surface tension and internal circulation—both properties modified by nanoparticle [38] and surfactant impurities [6]. Because terminal velocity arises when gravitational and drag forces are balanced, vertical wind tunnels provide a controlled means of replicating these conditions by counteracting gravity with upward airflow, enabling stable drop levitation. The effects of surfactant on the behavior of levitating drops have been studied in vertical wind tunnels, with the reduction in surface tension resulting in reduced internal circulation, reduced oscillation, and increased flattening of the drop [6,39]. The effect of nanoparticles on the behavior of levitating drops is, to our knowledge, absent from the literature despite the relevance of nanoparticles and surfactants in both environmental and industrial applications.

Vertical wind tunnel designs have gradually evolved to enable suspension of progressively larger drops. Early tunnels were limited to small drops (<0.5 mm), which could be stabilized near the tunnel center [40]. The University of California Los Angeles (UCLA) cloud tunnel extended these capabilities to drops in the typical raindrop size range (0.2–6 mm) [41,42]. Experiments in this facility revealed that larger drops exhibited a linear decrease in resistance to lateral deformation [12], whereas smaller drops remained comparatively stable. In addition, drops displayed well-developed internal circulation consistent with external flow patterns [12]. Using snapshot imaging, researchers are able to document deformation, nucleation, and oscillatory behavior.

Beard and Kubesh (1991) describe drop oscillation as modes composed of spherical harmonic perturbations, with frequencies dependent on order n [43]. Oscillations allow for degenerate modes $m = n + 1$. The notation (n, m) has been used to describe distinct oscillation modes [5,39,43–45]. Drops greater than a threshold diameter (>1 mm) are shown to primarily oscillate at three oscillation modes: axisymmetric ($n = 2, m = 0$), horizontal (2,2), and transverse (2,1) [43], each with a unique spatial residence in two dimensions (2D). This threshold arises as the aerodynamic force

and liquid weight that deform the drop exceed the surface tension that stabilizes the spherical shape of the drop, making the drop shape flattened and deviating from a liquid sphere [6]. Higher-order oscillation modes, such as $n = 3$, have been previously thought to be nearly undetectable past this threshold where the $n = 2$ mode dominates [5]. As surface tension is dependent on drop composition [6], this threshold is also flexible. The axisymmetric mode consists of drop oscillations about the vertical axis, the horizontal mode is usually lower frequency and occurs along the horizontal axis, and the transverse mode is defined by high-frequency oscillations at an inclination angle of $\pm 45^\circ$ from the horizontal axis. More recently, these theoretical results have been reproduced at the Mainz vertical wind tunnel [5,44]. Novel techniques, such as analyzing the beating response of axisymmetric oscillations over time, provided experimental validation of the predicted oscillation modes [39]. Drops containing surfactants, which reduce surface tension, were also examined and found to undergo greater deformation and lower oscillation frequencies [39].

In this work, we investigate the influence of varying concentrations of nanoparticles and surfactant on hydrometeor behavior. Nanoparticle concentrations of 0.1%, 0.5%, and 1% silicon dioxide are employed. The concentrations we investigate are greater than those typically encountered in the atmosphere. The concentration of silicon dioxide nanoparticles in atmospheric precipitation has not been widely explored, to our knowledge, but we surmise the concentrations of nanoparticles in raindrops are orders of magnitude lower than those we test here. The estimated concentration of silicon dioxide nanoparticles in surface water is relatively low (7×10^{-11}%) [46] and may be used as a lower estimate. Higher concentrations are found in urban and industrial centers [47,48] in excess of ∼3 times those in rural counterparts, a likely consequence of industrial processes that exacerbate levels of atmospheric nanoparticles [49]. Products containing silicon dioxide nanoparticles such as household cleaning products and spray coatings host a greater concentration and can vary widely depending on the application. For instance, certain window cleaning agents may have concentrations of ≈0.09–0.3% [50], whereas the levels in food and paint coatings may reach 2% [51,52]. Nanofluid studies routinely employ similar or higher nanoparticle loadings to magnify changes in bulk and interfacial properties, such as viscosity, thermal conductivity, and stability (e.g., Yalçın *et al.* found up to 3% silicon dioxide [53] and Rejvani *et al.* found up to 1.5% silicon dioxide [54]). Elevated concentrations of nanoparticles allow us to probe the limits of nanoparticle-drop interactions and identify behaviors that might remain undetectable at lower ambient levels. Moreover, elevated nanoparticle concentrations serve as analogues for artificial applications such as cloud seeding and industrial sprays, where local aerosol densities can exceed ambient levels by orders of magnitude [55,56]. Simulations of artificial seeding have shown aerosol concentrations in seeded plumes in the range ~ 1–1.8×10^4 cm^{-3} [57], far above typical background aerosol concentrations of ≈ 750 cm^{-3} in polluted air [58]. Our concentration regime balances experimental sensitivity with applied relevance, allowing us to explore extreme hydrometeor-nanoparticle dynamics that lie at the intersection of theory and practice.

A relatively well-studied industrial surfactant (Triton X-100) is introduced at a constant concentration (0.02%) to reduce surface tension in both distilled water and nanofluid drops. Drops are levitated in a vertical wind tunnel across a diameter range ($D_0 \approx 1$–7 mm) and their deformation, oscillation, and stability characteristics are analyzed.

II. METHODS

A. Vertical wind tunnel design

A schematic of our vertical wind tunnel is shown in Fig. 1. An 8-inch duct fan pushes air through a 0.05-μm HEPA filter and two layers of 0.5-in honeycomb laminarizers with 0.125-in cells. The laminarized flow exits the honeycomb and is contracted. The resulting velocity into the viewing section is ≈10 m/s and variable based on fan speed. The half width f of the square contraction in centimeters is defined by $f(y) = -1.2 \times 10^{-7} y^6 + 8.9 \times 10^{-6} y^5 - 1.7 \times 10^{-4} y^4 + 15$, where y

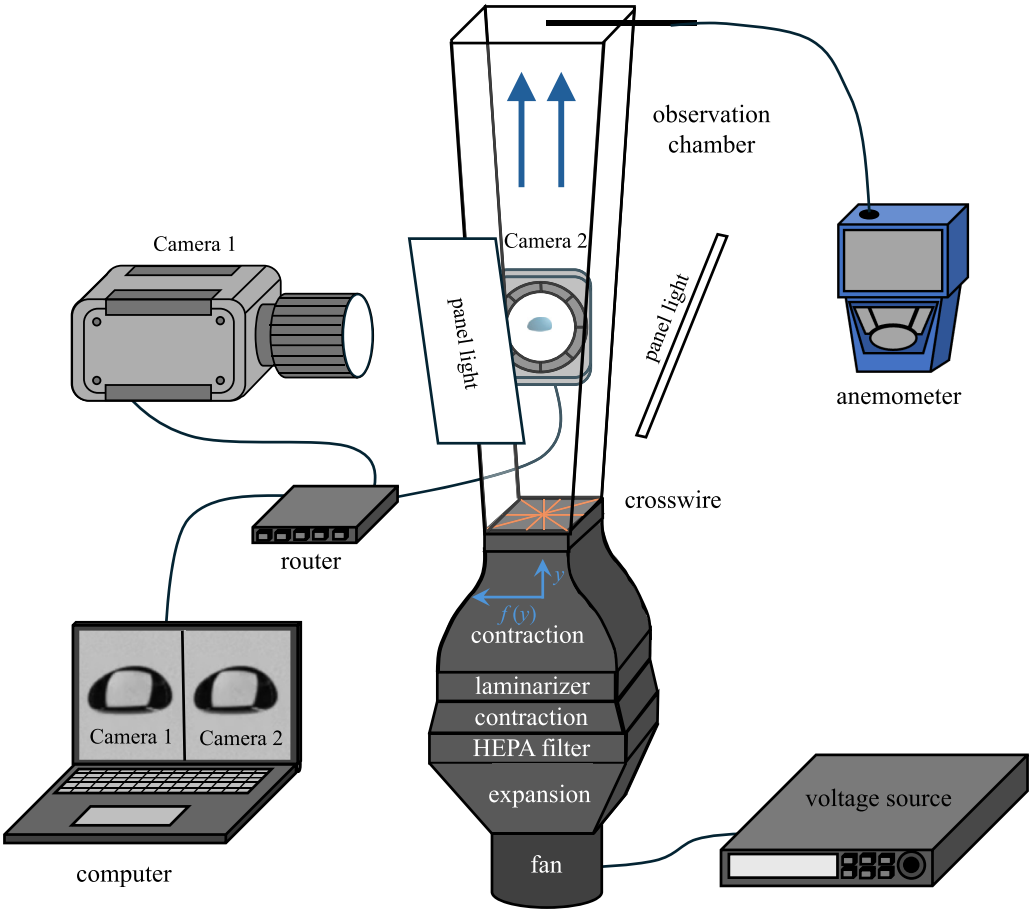

FIG. 1. Schematic of the experimental setup. Two synchronized high-speed cameras record a video of the drop levitating in the vertical wind tunnel. The router ensures synchronization of the two cameras which can simultaneously be viewed in a computer. The voltage source is used to control the airflow from the fan, measured by an anemometer at the exit. Blue arrows indicate the direction of airflow in the tunnel.

(cm) is the axial dimension of the contraction and $y = 0$ corresponds to the contraction inlet, the same contraction chamber profile used in a previous study [59].

The cross-sectional area of the observation chamber linearly increases from inlet (120 × 120 mm) to outlet (120 × 150 mm), 70 cm downstream, at an area ratio of 1.25, resulting in a vertical velocity gradient—heavier drops will levitate lower in the observation chamber at fixed fan speed. A crosswire at the inlet of the observation chamber formed by eight 80-μm-diameter wires creates a radial velocity gradient that stabilizes levitating drops at the center of the wind tunnel cross section [60]. Vorticity and turbulence intensity is calculated using SOLIDWORKS [61] flow simulations at 273 K, inlet velocity 8 m/s, and pressure 101.32 kPa. The velocity well retains similarity across the tunnel span (l) traveling axially away from the crosswire (h), as shown in Fig. 2(a). Vorticity is very low in the tunnel core and largest in the nominally laminar boundary layer, as shown in Fig. 2(b). Fan speed is modulated by an Itech IT-M7721 variable AC voltage source and windspeed measured by a Koselig HT-9830 anemometer. The flow speed U is calculated by correcting anemometer readings according to the stable drop levitation volume in view of our cameras. Tunnel velocity measurements are triplicated, with an average standard deviation in flow speed of ±0.070 m/s.

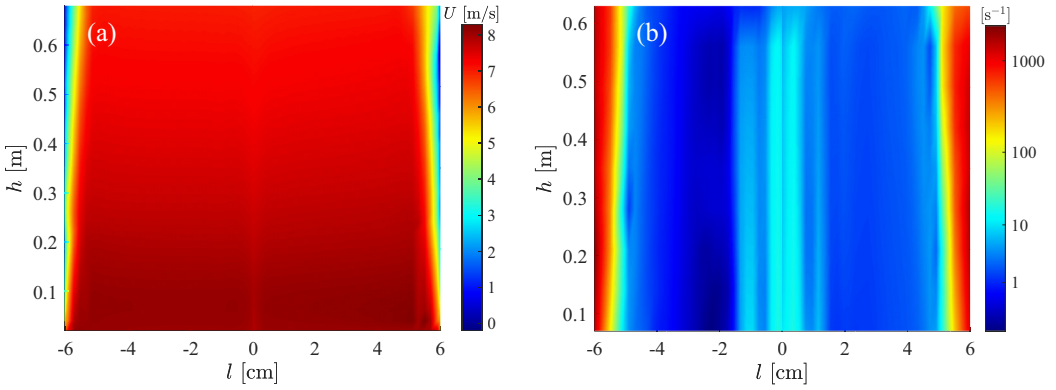

FIG. 2. (a) Velocity and (b) vorticity maps of simulations along the height h and width l of our vertical wind tunnel. The inlet velocity is 8 m/s.

Drops are released from straight-cut needles placed normal to the air flow above the wind tunnel. We use three different needles with internal diameters 1.6, 1.19, and 0.84 mm.

Drop analysis is typically done for $(10^{-1} - 1)$ s windows because the high frequency of drop oscillation permits brief times. However, these short analysis durations are not representative of the tunnel's capability to levitate drops for many minutes. In practice, the limiting factor for drop levitation time is drop evaporation, rather than instability in drop position. In principle, the vertical velocity gradient and radial centering flow permit indefinite levitation until complete vaporization. In practice, we are limited by the size of the wires generating the velocity well to a drop diameter of $\gtrsim$2.5 mm.

Such a capability to observe drops for multiple minutes sharply contrasts with high-speed optical disdrometers and 2D video disdrometer systems, which observe freely falling drops for $O(10)$ milliseconds as they pass through an observation volume [62]. As a result, disdrometer-based measurements necessarily capture much shorter snapshots of drop dynamics than our tunnel. After release from the injection needle, drops typically require less than one second to reach a steady equilibrium position within the chamber. All high-speed imaging, measurements, and analyses presented in this work are performed multiple seconds after this transient period. As a result, all reported measurements are independent of the transient effects associated with drop injection and the establishment of stasis in the tunnel, a point we justify further below. The small vertical position jitter observed in Fig. 3 reflects low-amplitude fluctuations about an equilibrium levitation position.

B. Preparation of fluids

Eight liquid solutions with varying volumetric concentrations of silicon dioxide and Triton X-100 surfactant were prepared as listed in Table I. Nanoparticles may be adequately dispersed to prevent coagulation in a liquid medium by magnetic stirring at ≈400–800 rpm followed by sonification for 30–60 mins [63,64]. Nanoparticles and silicon dioxide, in particular, amalgamate in a time span ranging from minutes to days depending on base fluid, temperature, and particle size [65]. Nanoparticles are prone to amalgamation in both environmental sources in static and dynamic water [66], as well as in industrial sources such as paint [11]. We seek to mimic the incomplete nanoparticle dispersion that would be seen in such sources to investigate influences on drop properties such as oscillation. Thus, fluid solutions were mixed with a magnetic stir for at least 90 min at 340 rpm, then sonicated for 32 min. All experiments were done within 24 h after the solution has been made—with fluid solutions kept in a magnetic stir at 340 rpm during storage.

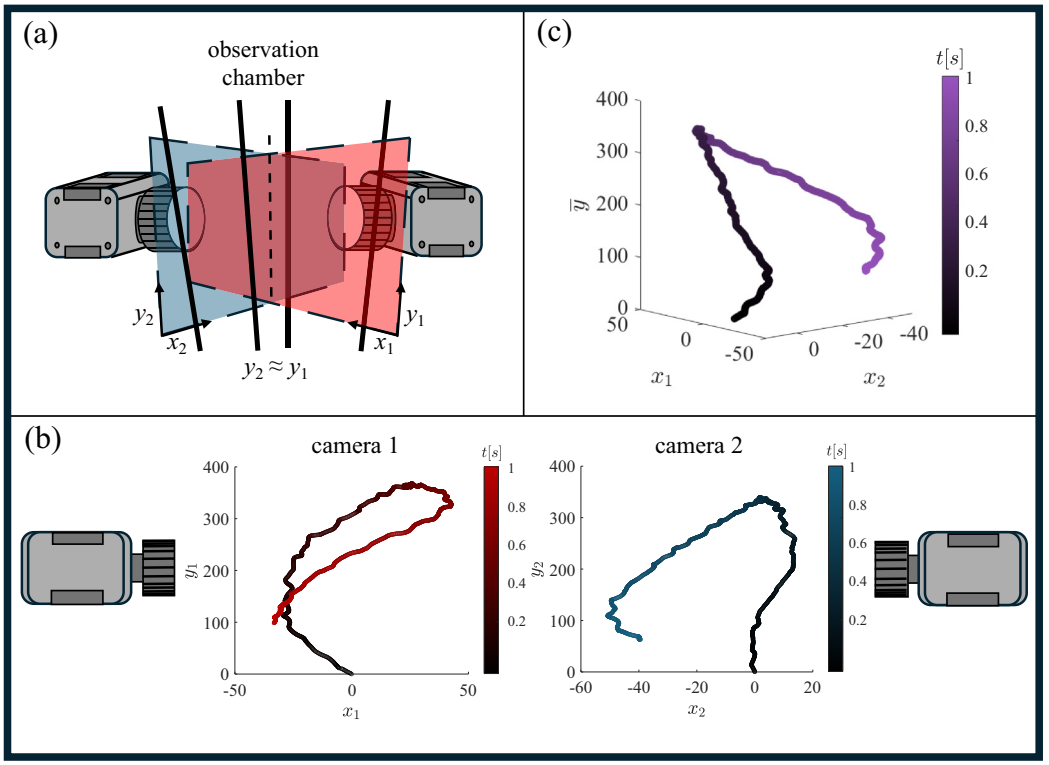

FIG. 3. 3D tracking of the drop using two synchronized cameras. (a) Two orthogonal and synchronized high-speed cameras 1 and 2 record a video of the drop levitating in the vertical wind tunnel. (b) 2D tracking of the drop from each side camera. (c) 3D tracking of the drop using the 2D plots in (b).

C. 3D tracking with two cameras

Two synchronized, orthogonally placed Photron Nova S6 high-speed cameras record videos of a levitating drop ($N = 72$) at 2000 fps and resolutions 10.70 ± 0.07 pxl/mm for Camera 1 and 10.35 ± 0.05 pxl/mm for Camera 2, as shown in Figs. 1 and 3(a). Experimental drops have Reynolds number $\mathrm{Re} = \rho_a U D_0/\mu_a = 1803$–$4102$, Weber number $\mathrm{We} = \rho_a U^2 D_0/\sigma = 4184$–$11\,477$, and Bond number $\mathrm{Bo} = U/\sqrt{gD_0} = 2.1$–$10.9$, where σ is surface tension and g is the acceleration of gravity. Resolutions for each camera are a mean of the calculated resolution ($N = 8$) of centimeter

TABLE I. Experimental fluids. $N = 3$ for surface tension measurements and $N = 10$ for viscosity measurements.

Description	Surface tension [mN/m]	Viscosity [mPa s]
Distilled water	69.8 ± 1.1	1.131 ± 0.004
0.02% Triton X-100	30.9 ± 1.5	1.136 ± 0.004
1% SiO_2	77.1 ± 2.4	1.174 ± 0.003
1% SiO_2, 0.02% Triton X-100	33.5 ± 3.0	1.179 ± 0.005
0.5% SiO_2	72.9 ± 4.0	1.164 ± 0.005
0.5% SiO_2, 0.02% Triton X-100	31.7 ± 2.3	1.183 ± 0.004
0.1% SiO_2	65.0 ± 1.0	1.138 ± 0.005
0.1% SiO_2, 0.02% Triton X-100	28.4 ± 3.6	1.147 ± 0.005

markings along a vertically suspended metric ruler at both the closest and farthest locations in the observation window relative to each camera. Two light panels across each camera backlight the levitating drop. Each camera is used to perform a 2D track of the drop, as shown in Fig. 3(b).

Such a conformation is inspired by *in situ* two-dimensional video distrometers (2DVD), used in estimating precipitation rate, distribution of drop sizes, and individual drop terminal velocities under low-wind conditions [67]. In our setup, where the drops remain very close to the center and the cameras are placed at a focal length to the sample drop, the distortion along each viewing plane is negligible ($<1\%$). The NIKKOR 24–120 mm f/4G ED VR lens extensions on the cameras are placed $\approx$543 mm away from the center of the observation chamber. Given a 0.020 mm circle of confusion, a focus 543 mm away retrieves a maximum depth of field of 490 mm. The far and near limits are 889 and 391 mm away from the cameras, respectively. From our vertical wind tunnel geometry, the maximum distance a drop may travel in the anteroposterior axis is 150 mm, well within the maximum depth of field of 490 mm.

Drops are detected using adaptive threshold binarization. For videos lacking sufficient contrast, Otsu's method and noise reduction techniques such as Wiener's method are performed [68]. The synchronized 2D data of the sample drop from each viewing plane can be used to track the position of the drop in 3D, as shown in Fig. 3(c).

D. Measurements

The flattening of hydrometeors under the influence of gravity and aerodynamic drag results in an disklike shape [5,6,13]. Deviations from such a shape result in an overestimate of the drop volume. Previous wind tunnel studies characterize drop volume by calculating the diameter of a sphere, with volume corresponding to the measured mass of the drop [5,39]. We assume radial symmetry and use the binarized drop shadow in the two viewing planes to reconstruct a volume via disk integration. A spherical equivalent diameter is calculated from the volume and time averaged as the volume equivalent diameter $\overline{D}_{\mathrm{v}}$, averaged across the two cameras. The volume is calculated from the area projections by assuming radial symmetry in each camera. We also provide another estimate of the spherical equivalent diameter calculated from the area and time averaged as the surface equivalent diameter $\overline{D}_{\mathrm{a}}$, averaged from the two cameras. While the shape of the drop is generally described as a disk, a disk cannot capture the changing shapes of the drop through time.

We form an aggregate heatmap image of the drop from its shadow as viewed in one camera through time, shown in Fig. 4(a) (see Movie S1 in the Supplemental Material [69]). Brighter regions indicate a greater degree of spatial residence. The average number of active pixels across all frames is recorded as N. The aggregate shape image, represented by the matrix I_0, is trimmed to a binarized characteristic shape image $I = 1(I_0 \geqslant k)$, where k denotes the value of the Nth largest pixel intensity. The resulting characteristic shape is shown in Fig. 4(b) (see Movie S1 in the Supplemental Material [69]). The characteristic shape presents average geometrical measurements relating to the drop shape and orientation, such as the ratio of the longest vertical chord to the longest horizontal chord or "axis ratio" α and the canting angle θ of the longest chord within the drop shadow with respect to the horizontal, as shown in Fig. 4(c). In our experiments, we find that the quantities derived from the characteristic shape are nearly equal to the time-averaged quantities of the levitating drop. For example, the time-averaged axis ratio of the levitating drop is plotted against the axis ratio of the characteristic shape with a nearly identical correspondence, as shown in Fig. 4(d). Thus, the characteristic shape represents the equilibrium drop shape and is robust to binarization challenges due to light refraction as the drops oscillate. Using the characteristic shape, we determine the major and minor axis, horizontal and vertical axes, and the equivalent diameter viewed in Camera 1 and Camera 2. The major and minor axes are defined as the corresponding axes of an ellipse that has the same normalized second central moments as the drop projection onto the viewing plane. The horizontal axis is the length of the maximum horizontal chord along the drop shadow and the vertical axis is the length of the maximum vertical chord along the drop shadow. A list of measurements obtained from our drop levitation experiments is provided in Table II.

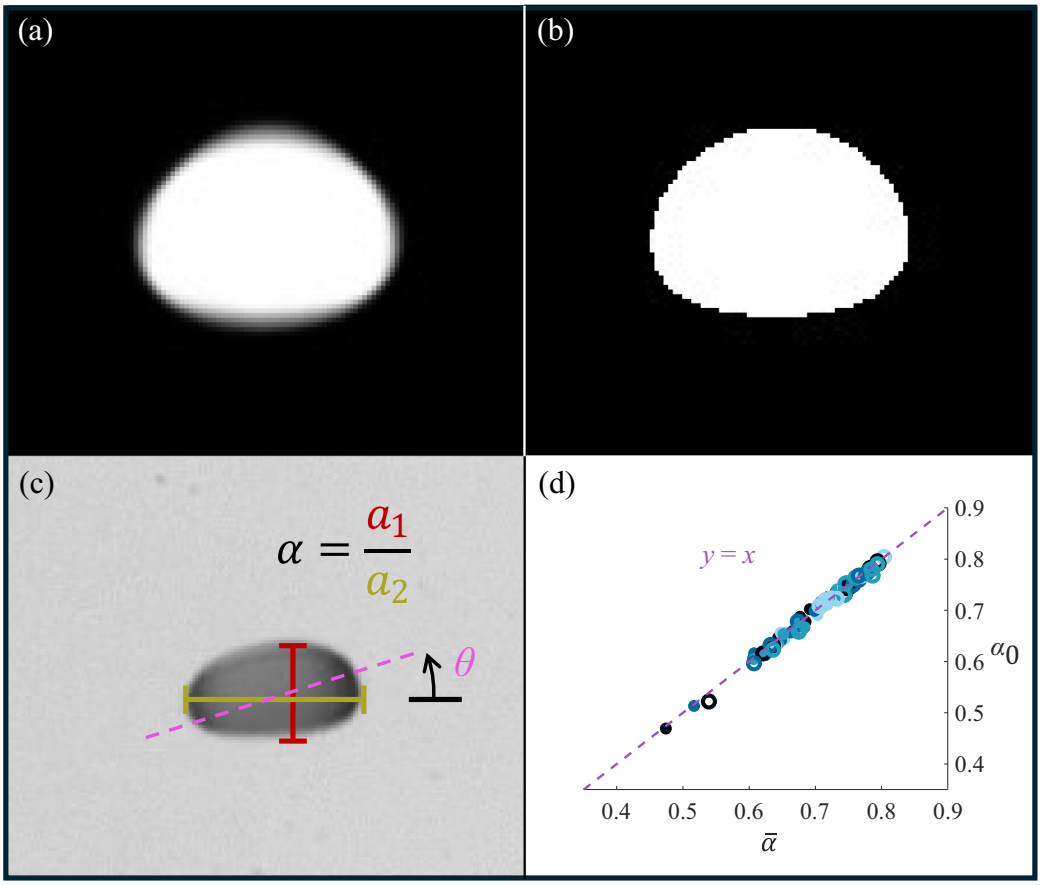

FIG. 4. (a) Aggregate shape of a drop levitating for 2 s. (b) Characteristic shape resulting from the aggregate shape in (a). (c) Calculating the axis ratio α and canting angle θ with respect to the horizontal axis. (d) The axis ratio of the characteristic shape α_0 is plotted against the time-averaged axis ratio over time $\bar{\alpha}$; the average standard deviation across trials, taken across all frames for each trial, is 0.08 ± 0.03 for $\bar{\alpha}$.

While falling drops are highly dynamic, it is possible to mathematically define a static, equilibrium drop shape, which preserves drop volume while balancing internal hydrostatic pressure with external aerodynamic pressure. The most prominent equilibrium drop shape model is that of Beard and Chuang [70]. Wind tunnel studies of drops with reduced surface tension support the Beard and Chuang model by comparing model shapes with shadow graphs of levitating drops [39]. Establishing an equilibrium drop shape permits the representation of a drop devoid of oscillation, and time-averaged measurements of a drop, such as axis ratio, also remove such oscillations. We aim to derive the equilibrium drop shape from still frames of the oscillating drop.

Drop shape is quantified with equal volume spherical diameters. Four such diameters are derived based on drop area D_a, estimated single-camera volume D_v, estimated dual-camera volume D_e, and the characteristic shape D_0. Unlike the characteristic shape diameter D_0, the area equivalent D_a, volume equivalent diameter D_v, and elliptical equivariant diameter D_e are determined for each individual still frame. The average of all frames is the diameter of the recorded drop and is denoted by a bar accent $\overline{\square}$.

The area equivariant diameter D_a is derived from the equal volume circle of the drop shadow. The volume equivalent diameter D_v is derived from the equal volume sphere of the disk, i.e., the integrated drop shadow along its vertical axis. Both methods are averaged across all frames in the

TABLE II. Nomenclature.

Measurement	Definition
Vertical axis (a_1)	Maximum continuous distance from the topmost to the bottommost point on the drop along a constant ordinate value as viewed on a camera plane
Horizontal axis (a_2)	Maximum continuous distance from the leftmost to the rightmost point on the droplet along the horizontal axis
Axis ratio (α)	Instantaneous ratio of horizontal axis to vertical axis
Characteristic axis ratio (α_0)	Ratio of horizontal axis to vertical axis on the characteristic shape averaged between Camera 1 and Camera 2
Minor axis (A_1)	Minor axis of the ellipse that has the same normalized second central moments as drop projection onto the viewing plane
Major axis (A_2)	Major axis of the ellipse that has the same normalized second central moments as droplet projection onto the viewing plane
Modified axis ratio (α^*)	Ratio of major axis to minor axis
Area equivalent diameter (D_a)	Diameter of circle with same area as the drop shadow
Volume equivalent diameter (D_v)	Diameter of a sphere with the same volume as the cylindrical integration of the drop shadow
Elliptical equivariant diameter (D_e)	Diameter of a sphere with the same volume as the elliptical integration of the drop shadow with horizontal lengths from Camera 1 and Camera 2 acting as chords on the ellipse
Characteristic shape equivalent diameter (D_0)	Diameter of a sphere with same volume as the cylindrical integration of the characteristic drop shadow; averaged between Camera 1 and Camera 2
Drop terminal velocity (U)	Speed of the wind tunnel airflow during drop levitation as measured by the anemometer at the center of the wind tunnel exit
Canting angle (β)	Instantaneous canting angle
Surface tension (σ)	Liquid surface tension
Nanoparticle concentration (C)	Nanoparticle concentration (% m/m)
Time average ($\overline{\square}$)	Bar accent indicates a time-averaged quantity
Nondimensionalized oscillation amplitude ($\breve{A}_x$)	The subscript indicates the mode of oscillation: A for axisymmetric, H for horizontal, and $n = 3$ for higher-order modes
Nondimensionalized total oscillation amplitude ($\breve{A}$)	Sum of $\breve{A}_A$, $\breve{A}_H$, and $\breve{A}_{n=3}$

trial and between the two cameras to produce $\overline{D}_a$ and $\overline{D}_v$ to represent the equilibrium drop diameter. The elliptical equivariant diameter D_e is derived from an equal volume sphere of the sum of single-pixel-thick elliptical prisms with chord lengths from both camera views. D_e may also be averaged over across all frames to produce $\overline{D}_e$.

The characteristic drop shape provides an approximation to the equilibrium drop shape and can provide drop measurements from a single image. Thus, an agreeable approximation of the diameter from the characteristic shape supports its use as a representation of the equilibrium drop shape. The volume of the characteristic drop is approximated as $V_0 = \pi \int_{y_0}^{y_1} [r(y)]^2 dy$, where r is half the length of active pixels along the horizontal axis of the drop at a given vertical coordinate y. The vertical axis is denoted by y, with y_0 and y_1 as the lower and upper coordinates of the drop, respectively. Computationally, the volume is the sum $V_0 = h\pi \sum_{i=y_0}^{y_1} r_i$, where h is the height of a pixel. The characteristic drop diameter D_0 corresponds to a sphere of volume V_0. We estimate that binarization of the drop shadow is uncertain by one pixel, or $\Delta r = 0.1$ mm, in r_i. And so, the maximum uncertainty in volume for each row is $2\pi r_i \Delta r$. Considering the worst-case scenario of a spherical drop provide the maximum number of uncertain pixel rows, the uncertainty in

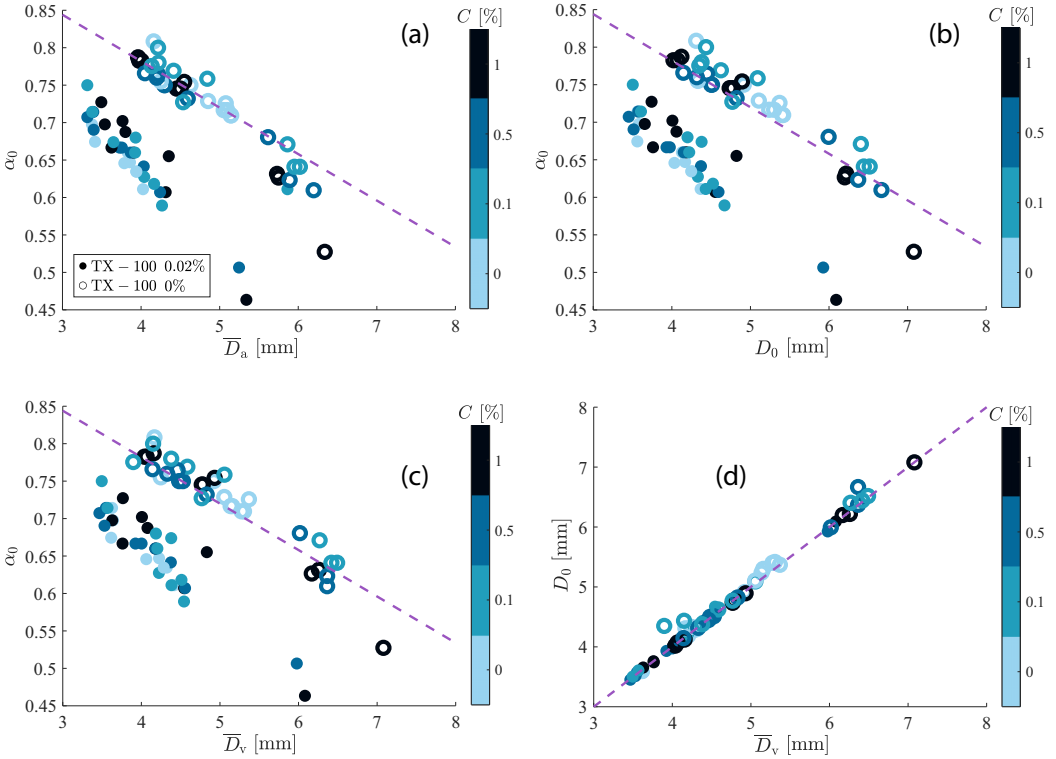

FIG. 5. (a)–(c) Purple dashed lines denote an empirical model ($\overline{\alpha} = 1.030$–$0.062D$) of axis ratio in terms of diameter from Beard *et al.* [71]. (a) Characteristic axis ratio α_0 plotted against time-averaged area equivalent diameter $\overline{D}_a$ ($r = 0.95$); the average standard deviation across trials, taken across all frames for each trial, is 0.15 ± 0.11 mm for $\overline{D}_a$. (b) Characteristic axis ratio α_0 plotted against characteristic diameter D_0 ($r = 0.95$). (c) Characteristic axis ratio α_0 plotted against time-averaged volume diameter $\overline{D}_v$ ($r = 0.95$); the average standard deviation across trials, taken across all frames for each trial, is 0.10 ± 0.10 for $\overline{\alpha}$. (d) Characteristic diameter $\overline{D}_0$ plotted against time-averaged volume diameter $\overline{D}_v$ ($r = 0.995$) with $y = x$ curve in purple.

volume if each row were suffering the same error is $\Delta V_0 \approx \pi D_0^2 \Delta r$, which is the shell of the sphere, at one-pixel thick. The percentage error in the drop volume in this worst-case scenario is $\Delta V_0/V_0 \approx 6\Delta r/D_0$. For our smallest 3.5-mm-diameter drops, $\Delta V_0/V_0 < 17.1\%$ and decreases for larger drops. Since $D_0 = (6V_0/\pi)^{1/3}$, the corresponding error in diameter for the 3.5-mm-diameter drop is $\Delta D_0/D_0 \approx \Delta V_0/3V_0 = 5.7\%$. Larger drops are more prone to self-occlusion during deformation [71,72], an error we minimize by time averaging drop volume and characteristic shape.

Our results are consistent with a well-established empirical model published by Beard *et al.* [71], denoted by a purple line in Fig. 5: $\overline{\alpha} = 1.030$–$0.062D$, where $\overline{\alpha}$ is the time-averaged axis ratio and D is the equivalent diameter of the drop in millimeters. Darker colors denote higher nanoparticle concentrations. Filled circles (•) denote surfactant-laden drops, whereas unfilled circles (○) denote drops without surfactant. The characteristic axis ratio α_0, the ratio of the maximum vertical to maximum horizontal chord of the characteristic shape, is plotted against the calculated drop diameters in Figs. 5(a)–5(c).

All three calculation methods shown in Figs. 5(a)–5(c) have Pearson's correlation coefficients $r = 0.95$ for nonsurfactant drops. Our data are also consistent with the older well-established model published by Andasager *et al.* [72]. The fact that we can calculate the drop diameter using three different methods that align well with published models gives us confidence that our drop volume estimates are correct. Furthermore, the fact that $D_0 \approx \overline{D}_a$ ($r = 0.96$, $R^2 = 0.92$) and $D_0 \approx \overline{D}_v$

($r \approx 1$, $R^2 = 0.99$), as shown in Fig. 5(d), validates the characteristic shape as a good baseline for time-averaged geometrical measurements of the levitating drop. The characteristic diameter demonstrates robustness against deviations arising from rogue pixels and is therefore adopted as our preferred metric for drop size estimation. Assuming radial symmetry in its computation yields diameter estimates that exhibit strong agreement with empirical models. In contrast, the asymmetric volume-equivalent diameters $\overline{D}_e$ tend to underestimate the model predictions, with the discrepancy increasing for larger drops, as discussed in Sec. 1 of the Supplemental Material [69]. A plot of α_0 against the volume-equivalent diameter calculated using the elliptical volume integration $\overline{D}_e$ is shown in Fig. S1a, and $\overline{D}_v - \overline{D}_e$ is plotted against the drop size in Fig. S1b in the Supplemental Material [69].

The "characteristic shape" that we define in Sec. II D, our attempt at a static drop representation, is in good agreement with time-averaged diameter $\overline{D}_v$, as shown in Fig. 5(d). Characteristic drop shapes obtained through binarization (white) well match the equilibrium shapes calculated by the Beard and Chuang model (black outline), shown in Fig. 6(a) for distilled water. Surfactant flattens the drop slightly beyond the model prediction, as shown in Fig. 6(b). In contrast, the addition of nanoparticles does not deviate the characteristic shape from the equilibrium shape, as shown in Fig. 6(c). Measurements of axis ratio α_0 quantify and support the observed distortion along the drop in Fig. 5(b). We thus demonstrate that an image that well characterizes the "equilibrium" or "characteristic" form of a drop can be realized with simple image aggregation.

III. RESULTS AND DISCUSSION

Drops in our vertical wind tunnel experience a radial velocity gradient and a vertical velocity gradient. The radial velocity gradient imposes greater flow at the drop edges than at the center, whereas the vertical velocity gradient imposes greater air velocity at the bottom of the wind tunnel. The radial gradient centers the drop within the tunnel cross section, whereas the vertical velocity gradient allows the drop to find vertical equilibrium or a zone thereof.

A. Nanoparticles do not alter drop shape

The drag coefficient [73] is

$$C_d = 2\frac{mg}{\rho_a U^2 S}, \tag{1}$$

where S is the projected surface area exposed to the ascending airflow, ρ_a is the density of air, g gravitational acceleration, and U is the terminal velocity of the drop. Mass m is determined from the density of the liquid drop and the estimated volume of the drop from disk integration of the characteristic shape. We have shown that D_0 follows the theoretical curves from previous published works in Sec. II D. Thus, the volume calculated from D_0 is approximately equal to the volume using disk integration, which may be used to calculate mass. Area S is calculated as the circular area of a diameter equal to the chord corresponding to the average horizontal axis of the characteristic shape in each camera view. A plot of the weight of the drop mg versus $\rho_a U^2 S$ is shown in Fig. 7(a), where C_d is proportional to the slope.

The coefficient of drag is a function of the Reynolds number $\mathrm{Re} = \rho_a U D_0/\mu$, where μ is the dynamic viscosity of air. The calculated C_d of our levitating drops (3–8 mm) is plotted against Re = 1803–4102 in Fig. 7(b). Filled circles (•) denote surfactant-laden drops, whereas unfilled circles (○) denote drops without surfactant. Redder hues indicate increasing axis ratio. C_d of raindrops increases with Re. Such an increase in C_d is in contrast to that of rigid spheres in the same diameter range, which decrease with Re. Goossens summarizes previously published models for the C_d of rigid spheres [74], which we include in Fig. 7(b). In the limit of $\alpha_0 \to 1$, the drop approaches a spherical shape and C_d approaches the predicted values for a rigid sphere. In the limit of $\mathrm{Re} \gg 1000$, the C_d of rigid spheres approach a constant value [75]. The relationship between

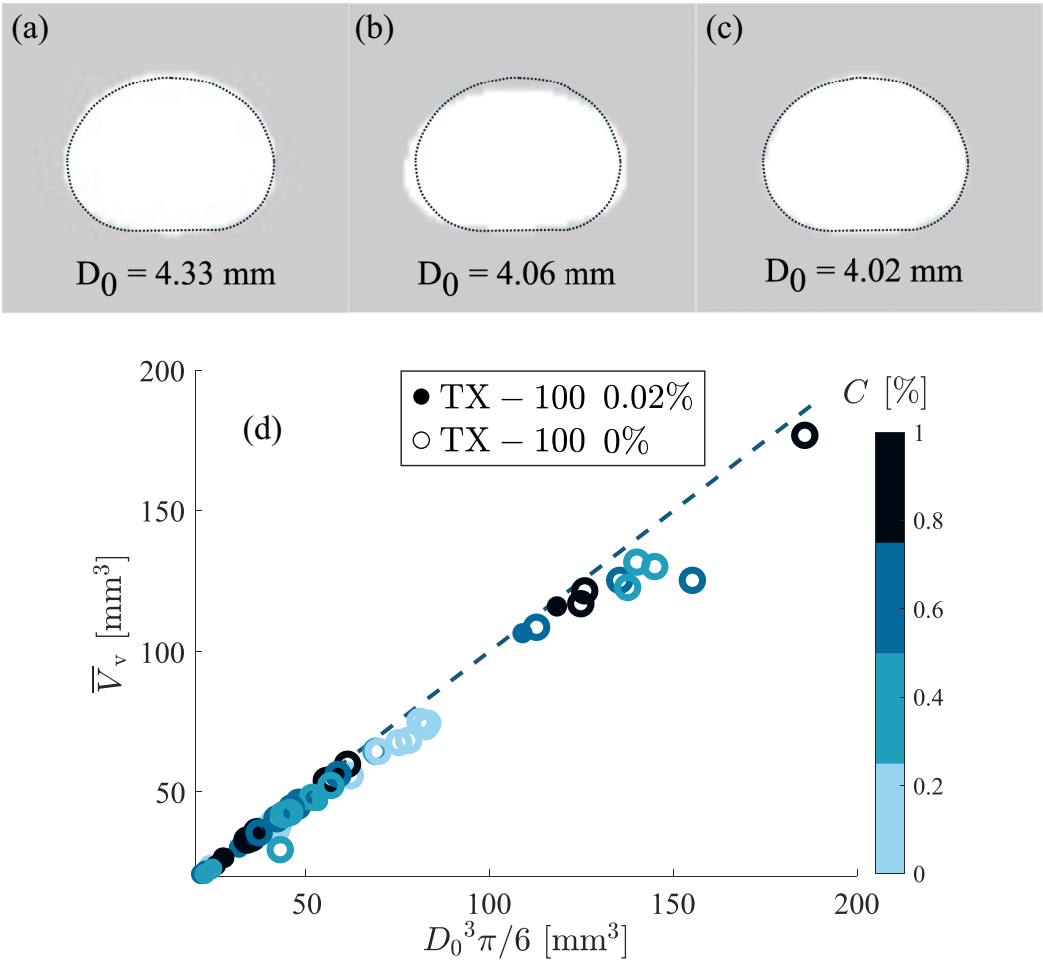

FIG. 6. Equilibrium drop parametrization for a pure water drop ($D_0 = 4$ mm) overlaid with the characteristic shape of (a) distilled water drop, (b) surfactant drop, and (c) nanoparticle drop ($C = 1\%$ m/m), and (d) time-averaged volume based on cylindrical integration $\overline{V}_v$ is plotted against the volume of the characteristic shape $D_0^3\pi/6$. The average standard deviation across trials, taken across all frames for each trial, is 4.57 ± 7.17 mm^3 for $\overline{V}_v$.

C_d and Re is approximately linear with $C_d = 0.00011\,\mathrm{Re} + 0.20$ (Pearson correlation coefficient $r = 0.93$) for drops without surfactant, consistent with the findings observed by Gunn and Kinzer for distilled water drops [37,76]. The addition of surfactant reduces the surface tension, allowing the drop to become flatter under the influence of aerodynamic drag, resulting in an increased $C_d = 0.0001\,\mathrm{Re} + 0.32$ ($r = 0.73$), as shown in Fig. 6(b). Surfactant increases the y intercept for the C_d linear fit, but the rate of change of C_d with respect to Re does not change when compared with drops without surfactant. Performing levitation experiments of distilled water drops with different levels of surfactant concentration will allow future researchers to obtain a relationship between the y intercept of C_d versus Re line and the surfactant concentration. Such a relationship is essential for improving drag models of contaminated or surfactant-laden drops, which are common in atmospheric and industrial aerosols [29–31]. Because nanoparticles do not alter the drop shape as discussed above, C_d is independent of nanoparticle concentration.

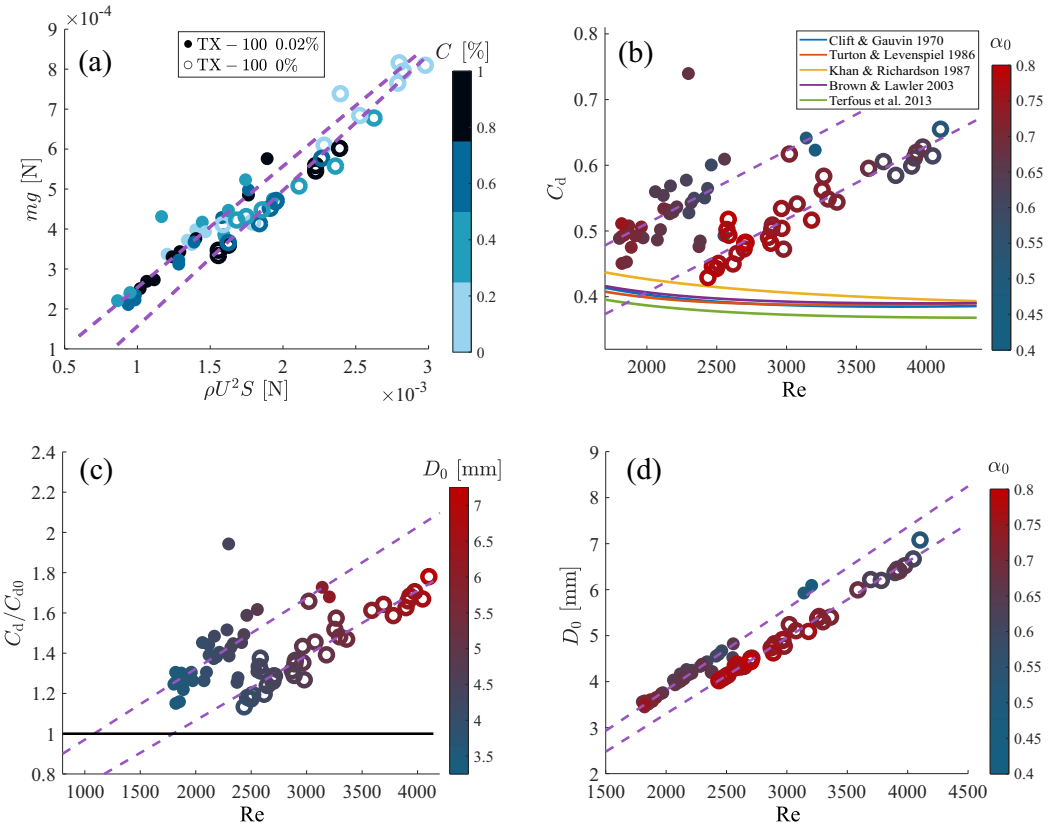

FIG. 7. (a) Weight of the drop mg plotted against $\rho_a U^2 S$ ($r = 0.997, 0.99$) so that the slope of the lines is proportional to the coefficient of drag. (b) Coefficient of drag C_d plotted against Reynolds number Re ($r = 0.93, 0.73$). Empirical models for the coefficient of drag for spheres are shown as colored lines. (c) Ratio of C_d to the coefficient of drag for a solid sphere C_{d0} plotted against Re ($r = 0.94, 0.80$). (d) Characteristic diameter D_0 plotted against Re ($r = 0.99, 0.98$). Lines are fitted using least-squares regression.

The ratio of C_d to the predicted coefficient of drag of a rigid sphere of the same size C_{d0} is plotted against Re in Fig. 7(c). The color gradient is based on the drop diameter D_0 instead of the characteristic axis ratio α_0. For the calculation of C_d/C_{d0}, we use a published model by Terfous *et al.*,

$$C_{d0} = 2.6689 + 21.683/\,\mathrm{Re} + 0.131/\,\mathrm{Re}^2 - 10.616/\,\mathrm{Re}^{0.1} + 12.216/\,\mathrm{Re}^{0.2}\,. \tag{2}$$

Because the drop size and shape determine the terminal velocity of a levitating drop, we achieve lower experimental values of Re by decreasing the drop size and adjusting the tunnel accordingly. As drop size increases, the ratio C_d/C_{d0} increases. We perform a least-squares linear regression to determine the value of Re from Fig. 7(c) and D_0 from a linear fit of D_0 vs Re where the drops achieve a perfectly spherical shape with $\alpha_0 = 1$ and $C_d/C_{d0} \to 1$. The linear relationship between D_0 and Re is shown in Fig. 7(d) with curves $D_0 = 0.00165\mathrm{Re} - 0.00129$ for drops without surfactant and $D_0 = 0.00177\mathrm{Re} + 0.27335$ for drops with surfactant (Pearson correlation coefficient $r = 0.99$ for both curves). As expected, surfactant increases D_0 for a given Re as the flatter shape of surfactant-laden drops allows for a greater surface area exposed to drag, resulting in greater lift force. Thus, drops with surfactant contain more volume at a lower terminal velocity compared with their counterparts that do not have surfactant. The value is Re = 1083 (2.19 mm drop) for our

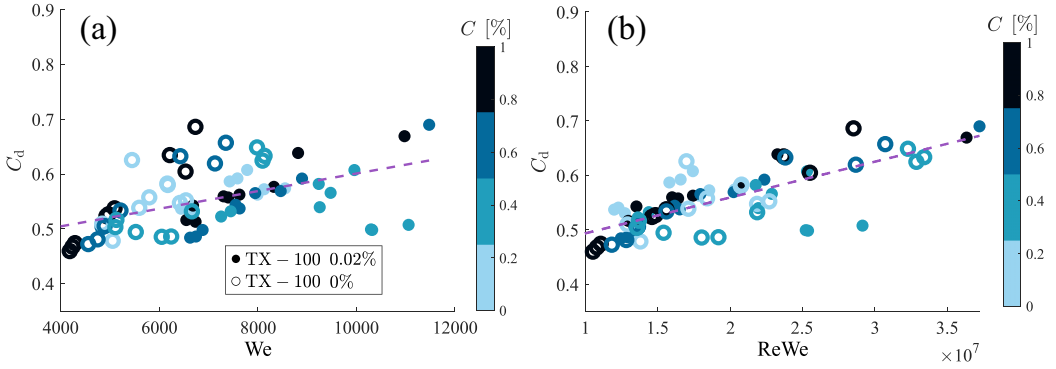

FIG. 8. Coefficient of drag C_d plotted against (a) We ($r = 0.50$) and (b) Re We ($r = 0.76$).

surfactant-laden drops and Re = 1794 (2.96 mm drop) for drops without surfactant. As expected, our surfactant-laden drops have a lower critical drop size for perfect sphericity, also seen in Fig. 7(c). As surfactant concentration increases, we expect the critical drop size to decrease. Our observations and methods to extrapolate the critical drop size for spherical behavior can be applied to drops with $D_0 \approx 1$–7 mm, which fall into the regime of small to large raindrops with an unsteady wake, as identified by Beard [76].

Surface tension effects on C_d can be interpreted through the Weber number, as shown in Fig. 8(a), which collapses the curves previously separated by surface tension in Fig. 7, but not completely as the Weber number does not account for the viscous effects in the surrounding airflow. We propose the product Re We by which to predict C_d, and plot the result in Fig. 8(b). Our proposed product is a superior predictor of C_d with correlation coefficient $r = 0.76$, compared with $r = 0.50$ for We. Such a combined parameter incorporates both aerodynamic inertial forcing and viscous transmission of stresses to the interface,

$$\text{Re We} = \left(\frac{\rho_l U^2 D_0}{\sigma}\right)\left(\frac{\rho_a U D_0}{\mu_a}\right) = \frac{\rho_a \rho_l U^3 D_0^2}{\mu_a \sigma}. \tag{3}$$

The result is a group that compares the magnitude of aerodynamic forces to viscous and capillary stabilization. In Eq. (3), the numerator consists of variables that promote deformation and flattening of the drop and consequently increase C_d. Increasing the air density ρ_a and air velocity U raise dynamic pressure. Larger drop diameter D_0 increases the area exposed to a dynamic pressure and lengthens the capillary restoration timescale, resulting in drop flattening and shape oscillations, which in turn increase C_d. The denominator consists of surface tension σ that promotes drop sphericity and air viscosity μ_a that dissipates momentum gradients in the surrounding flow, limiting the efficiency with which aerodynamic stresses deform the interface. Such quantities that promote drop sphericity and resist deformation naturally reduce C_d. In other words, Re We represents the balance between an aerodynamic impulse delivered to the drop and the viscous-capillary mechanisms that restore its shape. Increasing Re We results in greater deformation, flattening, and drag enhancement, whereas decreasing Re We results in more spherical drops.

The focal point of the cameras along the observation window lies approximately halfway between the inlet and the outlet bearing an anemometer in Fig. 1. Terminal velocity across drop size and nanoparticle concentration is plotted in Fig. 9(a). The terminal velocities of distilled water, with and without nanoparticles, appear independent of drop size and particle content in the $D = 4$–7 mm range. Plateauing of terminal velocities generally occurs at larger drop sizes due to flattening. Results from previous studies indicate a scattering of drop velocities as a result of unsteady wake [77], which is the regime for levitating drops of size $D_0 \approx 1$–7 mm as identified by Beard [78]. Terminal velocities of distilled water drops, regardless of nanoparticle concentration,

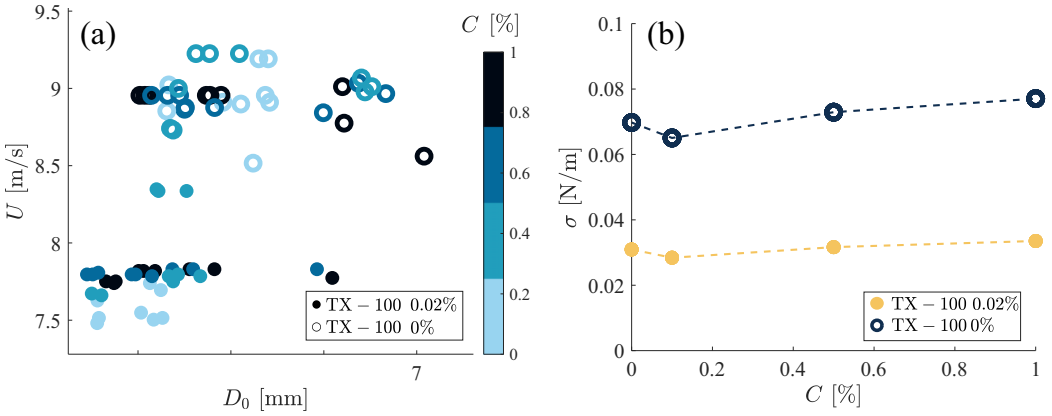

FIG. 9. (a) Terminal velocity U plotted against characteristic diameter D_0. (b) Surface tension of liquid σ plotted against NP concentration $C(\%)$. Surface tension values are provided in Table I.

remain tight, 8.5–9.2 m/s, a <10% variance with an average of $U = 8.95 \pm 0.141$ m/s. The addition of surfactant to distilled water significantly decreases the velocity to $U = 7.60 \pm 0.101$ m/s, while reducing scatter. In the presence of surfactant, nanoparticles increase U over those drops containing none. At concentrations >0.25% v/v, ∼5–15 nm silicon dioxide nanoparticles increase the surface tension of liquids [79,80], as shown in Fig. 9(b). The addition of nanoparticles neither affects the U nor the characteristic shape of drops without surfactant, as shown in Figs. 6(a) and 6(c).

B. Nanoparticles at low concentrations induce drop instability

As discussed in Sec. III A, the drop characteristic shape fails to express the specific dynamic changes that nanoparticles induce. Another metric that we use to demonstrate the excitation that nanoparticles incite is the canting angle β.

The canting angle is the angle of the drop major axis from the horizontal. An example of the time response of the canting angle is shown in Fig. 10(a). Analysis of the canting angle reveals excitation at the lowest concentration of nanoparticles (0.1% m/m). A plot of the time-averaged canting angular velocity $\overline{\dot{\beta}}$ versus the NP concentration is shown in Fig. 10(b). Lower nanoparticle concentrations (0.1% m/m) excite drop canting angular velocity in magnitude and scatter with and without the presence of surfactant ($25.5 \pm 11.7^\circ$ and $31.2 \pm 15.3^\circ$, respectively). The time average of the canting angle $\overline{\beta} \approx 0$. The activity of the canting angle can be quantified by taking the difference between the maximum and minimum canting angle $\Delta\beta$ for a 1-s period, coined the "amplitude" of the canting angle [5,39]. A plot of $\Delta\beta$ versus nanoparticle concentration is shown in Fig. 10(c). The addition of surfactant reduces $\Delta\beta$ when nanoparticles are present. In drops without surfactant, the addition of the lowest concentration of nanoparticles at 0.1% m/m is accompanied by an increase in average $\Delta\beta$ and standard deviation from $27.3 \pm 6.4^\circ$ to $43.8 \pm 25.6^\circ$, indicating increased drop deformation. In drops with surfactant, the addition of nanoparticles at 0.1% m/m increases the canting angle amplitude $\Delta\beta$ and standard deviation from $23.2 \pm 6.3^\circ$ to $40.3 \pm 36.1^\circ$. Once drops cross the vertical canting angle $|\beta| = 90^\circ$, the sign of the angle flips as the range of measurements for the canting angle are $-90^\circ < \beta < 90^\circ$, a phenomenon observed in large ($D_0 > 6$ mm) drops as a result of transient disturbances, as shown in Fig. 10(d).

At low concentrations of nanoparticles, their distribution on the liquid surface is nonuniform [81]. The patchwork in nanoparticle distribution results in local surface tension gradients that lead to increased deformation under flow [82], resulting in the excitation observed at 0.1% m/m silicon dioxide. The discrete patches of nanoparticles have larger surface tensions than the bulk and thus deform less than the neighboring, clean liquid. At nanoparticle concentrations (<0.5%),

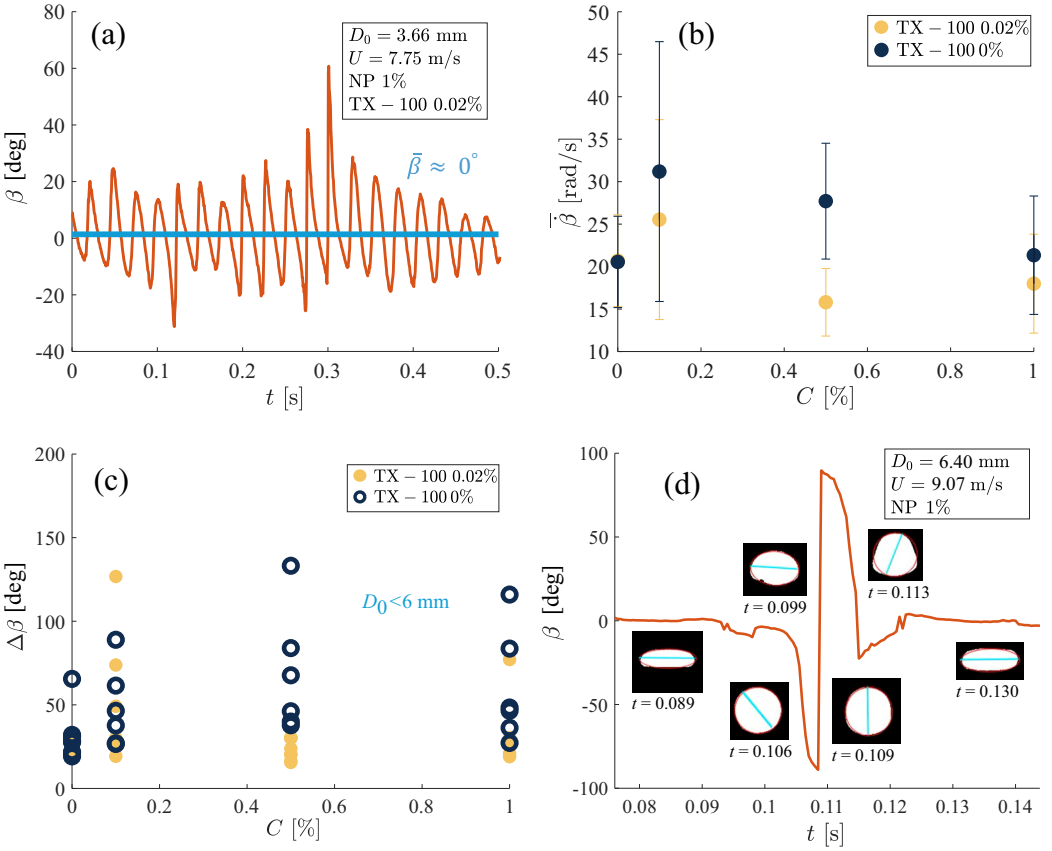

FIG. 10. (a) Canting angle β plotted against time t (orange); the time-averaged value for β is marked in blue. (b) Time-averaged canting angle angular velocity $\bar{\dot{\beta}}$ plotted against concentration nanoparticles C, where error bars correspond to the standard deviation. (c) Canting angle amplitude $\Delta\beta$ plotted against concentration nanoparticles C. (d) Canting angle β plotted against time t for a drop through a complete vertical circulation, a special case that occurs when $D_0 > 6$ mm, $C = 0.1\%$.

nanoparticles in liquid mixtures reduce surface tension [80], an observation that is also seen with silicon dioxide [79], which explains the observed dip in the surface tension at nanoparticle concentration $C = 0.1\%$ m/m observed in Fig. 9(b). Beyond a certain nanoparticle saturation concentration (NSC), the drop becomes saturated with nanoparticles and distribution on the fluid surface becomes increasingly homogeneous [83], resulting in diminishing changes to interfacial tension and increased drop shape stability, as indicated by reduced canting angle activity. Consequently, the reduction of $\Delta\beta$ by surfactants is diminished past the NSC, as shown in Fig. 10(c). In static microdroplets (diameter <50 μm) in microfluidic tubes, a particular study finds silicon dioxide to have a saturation concentration of ≈0.2% [83]; in our vertical wind tunnel where the drop is constantly being deformed, we expect the NSC to be higher as shown by the sustained decrease in surface tension, $C \approx 0$–0.5%, in Fig. 9(b) and sustained increase in β and $\Delta\beta$, $C \approx 0$–0.5%, in Figs. 10(b) and 10(c) as we suspect that the nanoparticles are continually being displaced from the surface to the drop interior. Increased deformation results in a lower time-averaged area normal to the airflow, resulting in the higher terminal velocity when compared to surfactant-only counterparts shown in Fig. 9(a). A true working NSC for levitating drops is unclear, though we believe it to be between 0.2% m/m and 0.5% m/m.

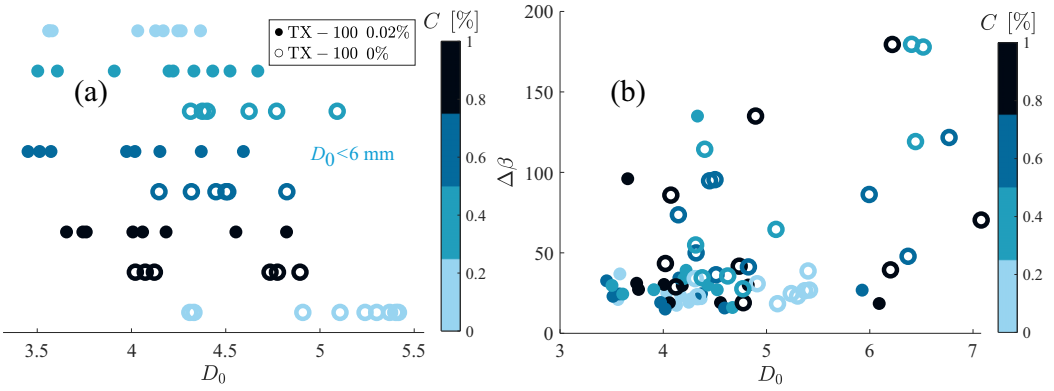

FIG. 11. (a) Diameter distribution of our trial drops. (b) Canting angle amplitude $\Delta\beta$ plotted against the characteristic drop diameter D_0.

At concentrations greater than the NSC, nanoparticles increase surface tension [79,84], saturate the drop surface [82,83], and decrease surface tension gradients, conferring increased interfacial stability. Stability reduces drop deformation, indicated by the reduced scatter in terminal velocity shown in Fig. 5(a), reduced scatter in $\Delta\beta$ shown in Fig. 10(a), and reduced canting angular velocity shown in Fig. 5(d), for nanoparticle concentrations 0.5% m/m and 0.1% m/m. At the highest concentration, the addition of surfactant produces negligible effects on $\Delta\beta$ and $\dot{\beta}$.

The effect of surfactant addition to nanoparticle solutions is dependent on concentration. The critical micelle concentration (CMC) of a surfactant is the concentration at which additional surfactant forms micelles within the fluid. For Triton X-100, this value is 0.22 mM [85] or ≈0.014% m/m. At surfactant concentrations beyond the CMC, surfactants participate in removing nanoparticles from the fluid interface. At low nanoparticle concentration (<0.5%), suppression of surface tension by nanoparticles is amplified by adding charged surfactants, especially at increasing concentrations relative to the critical micelle concentration [79]. Triton X-100 is a non-ionic surfactant. Thus, while our concentration of surfactant is 1.45 CMC, we do not see the solution to have the same synergistic decrease in surface tension described by previous works. Since the surfactant concentration used in our experiments is past the CMC, there are surfactant micelles that capture nanoparticles from the fluid surface [35]. Addition of surfactant prevents amalgamation [86], thereby discouraging possible surface tension gradients from forming and preventing drop deformation, which is seen in the reduction of the average canting angular velocity [Fig. 10(b)] and mean canting angle amplitude [Fig. 10(c)] at nearly all nanoparticle concentrations. As drops increase in size, inertial forces supersede surface tension, conferring decreased stability and increased deformation [5,71], allowing for the occurrence of complete vertical circulations, a phenomenon observed solely in large drops ($D_0 > 6$ mm), as shown in Fig. 10(d) (see Movie S3 in the Supplemental Material [69]).

Diameter effects are a key parameter when considering the results in Fig. 10. Our drop trials sit above 3.5 mm, keeping the diameter distribution tight overall (3.5–6 mm) across the window of analysis. The distribution of the solution types has overlap, especially at (4 to 5 mm), as shown in Fig. 11(a). Thus, when discussing data pertaining to the drop solution, we refer to the range of 3.5–6 mm, where diameter effects are superseded by the effects of drop composition.

Furthermore, the relationship between canting angle amplitude and drop diameter is seen in Fig. 11(b), which shows a dependence on drop diameter. The dependence of the drop diameter increases for drops approaching 6 mm and beyond, while drops below that threshold tend to show greater dependence on fluid composition than diameter.

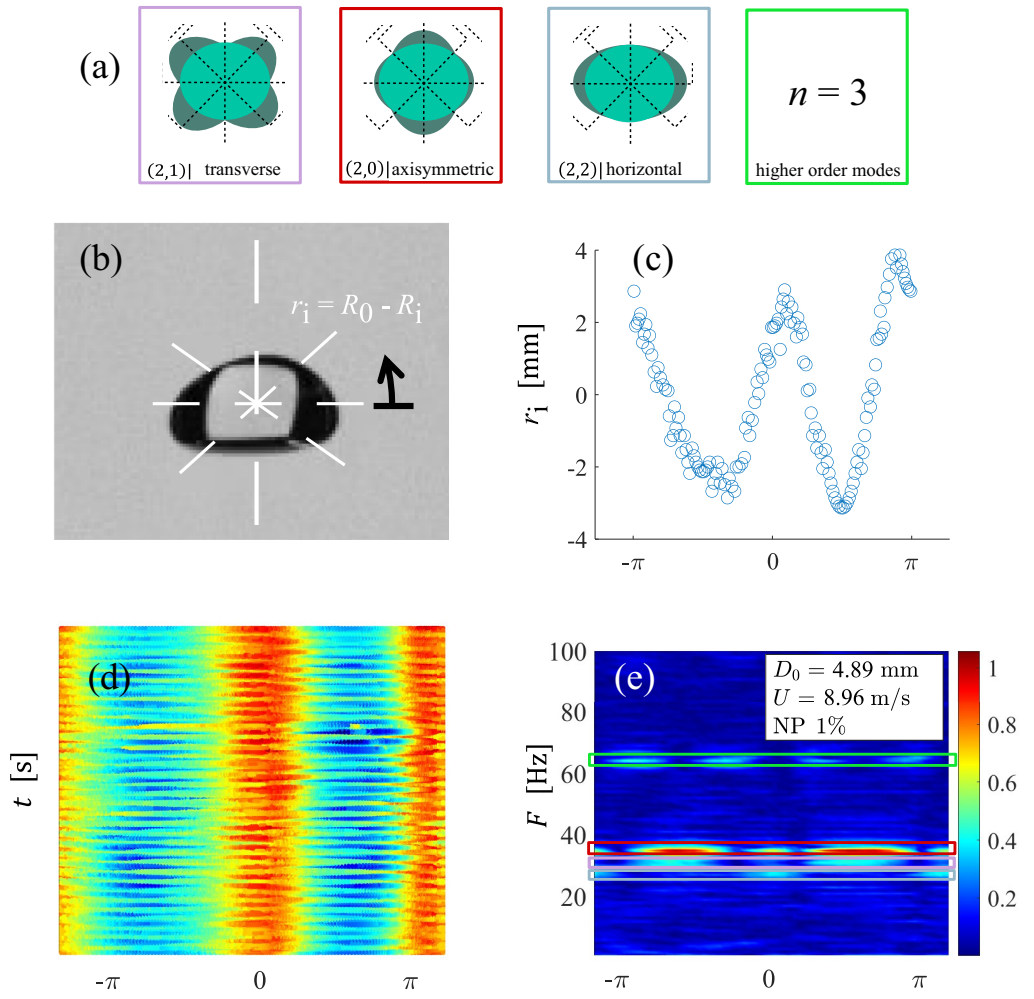

FIG. 12. (a) Dominant oscillation modes as observed from a 2D drop shadow. (b)–(e) Generation of frequency spectra for a ($D_0 = 4.89$ mm, $U = 8.96$ m/s, NP 1%) drop. (b) Drop schematic of radii differentials from the mean radii. (c) Plot of radii differentials r_i against angle for measurement. (d) Measurements shown in (c) across all recoded instances across trial. (e) Frequency spectra of drop oscillation along the radius of the drop. The colors of the boxes in (e) correspond to the modes in (a) which are boxed with the same color. The color bar shows the single-sided amplitude.

C. Surfactants suppress drop oscillation

Oscillation modes were first described for spherical liquid bodies by Raleigh, where drops have multiple degenerate modes $m = n + 1$ for each harmonic n [43,87]. For drops where deformation occurs ($D_0 > 1$ mm), the individual modes for each harmonic cease to be degenerate [5,43]. Larger drops also make higher-order harmonics ($n > 3$) harder to detect, often dominated by the quadrupole ($n = 2$) harmonic [13,39,76]. For $D_0 \approx 3$–6 mm, there exist three dominant modes [($n = 2, m = 0$); (2,1); (2,2)] observed in 2D from the drop shadow [43], shown in Fig. 12(a). The 3D models for the dominant oscillation modes have also been explored in previous works [45]. Detection of oscillation modes is often done by observing the frequency of the axis ratio for the axisymmetric oscillation mode which tends to be the most prominent [5].

While methods exist to determine individual oscillation modes [44,45], there are currently no published visualization tools that allow for viewing all oscillation modes observable from a given viewing plane, to our knowledge. Here, we present a method that graphically displays all oscillation modes of the levitating drop. A drop may be divided into N equivalent zenithal bins, as shown in Fig. 12(b) (see Movie S2 in the Supplemental Material [69]). Differential radii are taken for each bin $r_\mathrm{i} = R_\mathrm{i} - R_0$ as the difference between the radius at the bin R_i and the average radius around the drop shadow $R_0 = D_\mathrm{a}/2$ averaged across all frames, as shown in Fig. 12(c) (see Movie S2 in the Supplemental Material [69]). A given bin may contain multiple pixels. The possibility of multiple radii measurements per bin increases with pixels further from the centroid due to each bin occupying more space extending radially. If multiple data points exist in a given bin, the mean is used as R_i. Differential radii for all frames in a drop levitation video are plotted against the bin angle, as shown in Fig. 12(d) (see Movie S2 in the Supplemental Material [69]). The frequency response across each bin angle is computed, so that the plot in Fig. 12(d) is transformed to its frequency response spectrogram shown in Fig. 12(e) (see Movie S2 in the Supplemental Material [69]). The spectrogram allows for the instantaneous reading of all oscillation modes. Peak frequencies are extracted for two major modes and higher-order ($n = 3$) harmonic displayed in Figs. 13(a)–13(c) as the axisymmetric (2,0) and horizontal (2,2), as well as a higher-order harmonic ($n = 3$), respectively.

Models for the $n = 2$ harmonic are overlayed in Fig. 13(a). The models by Reyleigh [87] and Lamb [88,89] have degeneracies of the oscillation modes, while Feng and Beard [90] develop a closed-form solution for the nondegenerate oscillation modes of the $n = 2$ harmonic. For the axisymmetric oscillation mode, the models effectively overlay on top of one another, as seen in Fig. 13(a). Our results consistently show a greater frequency than predicted, an effect more pronounced with the fit to the reduced surface tension model. Our results confirm the transverse oscillation mode to be a slightly less, if not the same, frequency as the axisymmetric oscillation mode [6,44]. Only 57% of the trials hosted clear recovery of an independent transverse frequency, with its peak close to or compounding onto the axisymmetric oscillation frequency. The horizontal oscillation mode has a more distinct peak and was present in nearly all (94%) drops. The horizontal oscillation mode has great fit with both the nonsurfactant and the surfactant fits of the Feng and Beard model seen in Fig. 13(b). The frequencies of the higher-order ($n = 3$) harmonic are more erratic than the $n = 2$ modes. The retrieved frequencies are shown to fit well with the Rayleigh model seen in Fig. 13(c), though, as shown with the axisymmetric oscillation mode, it too shows a greater than predicted frequency, especially for drops with reduced surface tension.

As expected, larger drops have a lower oscillation frequency for all modes. The addition of surfactant reduces the oscillation frequency across all oscillation modes. We observe no effect of the addition of nanoparticles on the oscillation modes and frequencies of levitating drops. The frequency spacing between the $n = 3$ and the axisymmetric mode and between the $n = 3$ and horizontal mode is reduced by surfactant and drop diameter as shown in Figs. 13(d) and 13(e). The frequency gap between the horizontal and axisymmetric modes is increased by surfactant, but independent of drop diameter, as shown in Fig. 13(f).

The nondimensionalized amplitude of each oscillation is retrieved according to

$$\breve{A}_\mathrm{x} = \frac{\sum_i^N A_\mathrm{i}(F_\mathrm{x})}{ND_0}, \tag{4}$$

where $A_\mathrm{i}(F_\mathrm{x})$ is the single-sided amplitude on the ith radius bin along N bins at frequency F_x corresponding to the axisymmetric F_A, horizontal F_H, and $n = 3$ $F_{\mathrm{n=3}}$ oscillation modes. Each oscillation mode exhibits distinct behaviors, depending on the Reynolds number and nanoparticle concentration. $\breve{A}_\mathrm{x}$ is also sensitive to noise, especially along the transverse and horizontal oscillation modes. Individual modes and complications are further discussed in the Supplemental Material [69]. A nondimensionalized sum of amplitudes is described as follows:

$$\breve{A} = \breve{A}_\mathrm{A} + \breve{A}_\mathrm{H} + \breve{A}_{\mathrm{n=3}}. \tag{5}$$

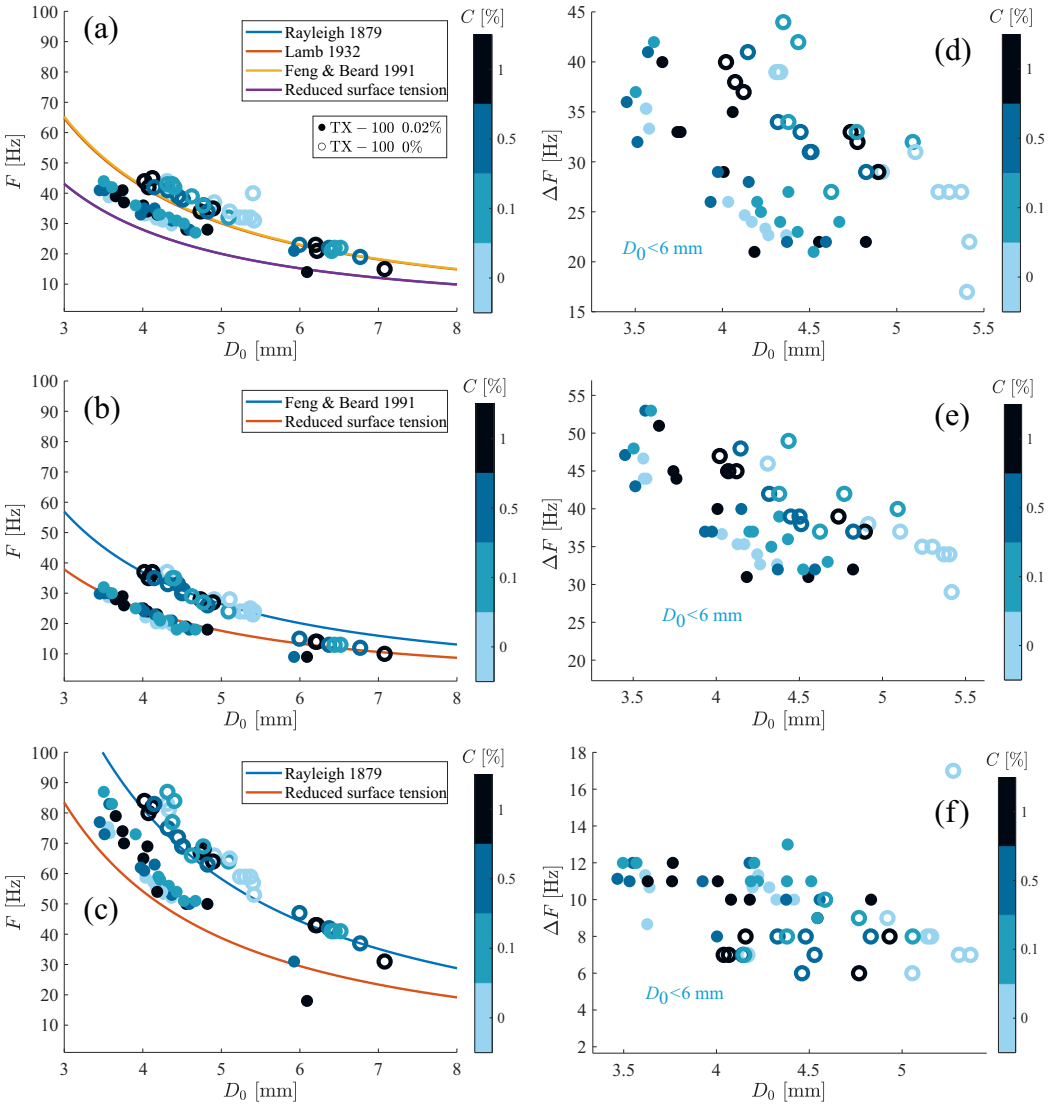

FIG. 13. (a) Average frequency F of axisymmetric oscillation mode against characteristic drop diameter D_0. (b) Average frequency F of horizontal oscillation mode against characteristic drop diameter D_0. (c) Average frequency F of higher-order ($n = 3$) oscillation mode against characteristic drop diameter D_0. (d) Frequency difference ΔF of $n = 3$ and axisymmetric oscillation mode against characteristic drop diameter D_0. (e) Frequency difference ΔF of $n = 3$ and horizontal oscillation mode against characteristic drop diameter D_0. (f) Frequency difference ΔF of axisymmetric and horizontal oscillation mode against characteristic drop diameter D_0.

The normalized amplitude $\breve{A}$ accounts for the oscillation amplitude along the three most prominent frequencies of the higher order ($n = 3$)$\breve{A}_{\mathrm{n=3}}$, axisymmetric $\breve{A}_{\mathrm{A}}$, and horizontal $\breve{A}_{\mathrm{H}}$, while also minimizing noise from improper recovery of $\breve{A}_{n=3}$ and $\breve{A}_{\mathrm{H}}$. Figure 14 shows $\breve{A}$ against a concentration of nanoparticles and Reynolds number. The axisymmetric amplitude $\breve{A}_{\mathrm{A}}$ is the most prominent and governs $\breve{A}$. Similar to $\Delta\beta$ and $\overline{\beta}$, nanoparticle drops reduce in magnitude past a certain NSC as nanoparticles become uniform on the drop surface, as shown in Fig. 14(a). We suspect a shift in the

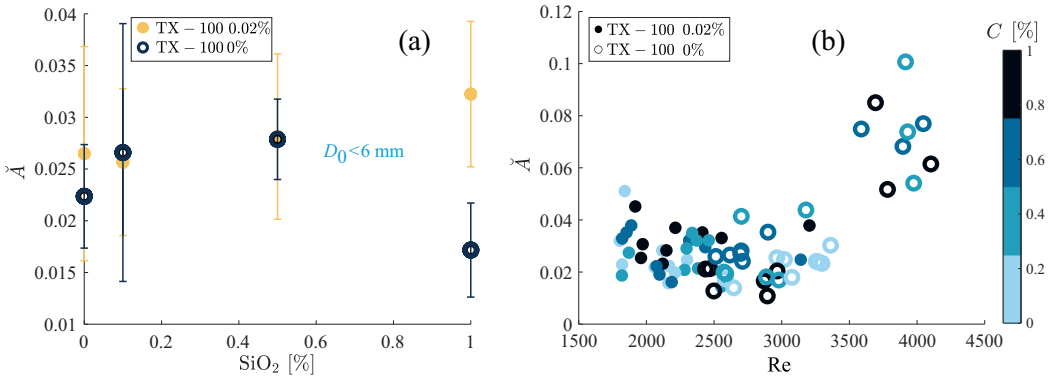

FIG. 14. Nondimensionalized amplitude sum $\breve{A}$ against (a) concentration of nanoparticles (error bars correspond to standard deviation) and (b) Reynolds number Re.

NSC from the addition of surfactant, resulting in a shift in maxima from 0.5% m/m nanoparticles to 1% m/m nanoparticles. Our surfactant concentration is beyond the critical micelle concentration and is likely capturing particles from the fluid surface [35]. Such an event would require more nanoparticles to saturate the fluid surface, thus shifting the NSC. The magnitude of $\breve{A}$ increases drastically for all drops greater than Re $\approx$ 3000 and gradually for drops less than Re $\approx$ 1800. Each individual amplitude $\breve{A}_x$ also increases beyond Re $\approx$ 3000 to varying degrees, as shown in the Supplemental Material [69]. At especially large diameters, such as those >5–6 mm, drops host increased deformation and even approach break up [70,91,92]. The 5 to 6 mm drops have Reynolds numbers Re = 3031–3637, according to our fit of drop diameter to Reynolds number. The drastic increase observed at Re > 3000 is likely due the increased instability of the larger drop as it approaches the threshold of breakup.

Excitation may be measured through the Womersley number $\mathrm{Wo} = D_0(2\pi F_A \rho/\mu)^{\frac{1}{2}}$, where F_A is the axisymmetric oscillation frequency and ρ and μ are the density and dynamic viscosity, respectively, of the fluid. Wo is a measure of excitation as it collapses the diameter and frequency, as shown in Figs. 15(a) and 15(b), where Wo is plotted against and $\breve{A}_A \Delta\beta$. When plotted against nanoparticle concentration in Fig. 15(c), there exists a bifurcation of surfactant and nonsurfactant trials at Wo = 60 independent of nanoparticle concentration; this indicates that Wo, and thus excitation, is influenced primarily by the presence of surfactant and not nanoparticles.

D. Two-dimensional camera view reveals drop orientation

A key consideration is whether the observed oscillation modes and canting dynamics are "steady-state" features of the levitated drops or transient remnants associated with drop formation at the injection needle. In our experiments, data acquisition is initiated only after the drop has reached a stable equilibrium position and orientation within the vertical wind tunnel, typically more than 1 s after release. This delay exceeds the characteristic timescale over which injection-induced disturbances decay, which is less than 1 s. We verify this notion by taking the average logarithmic decrement δ of our oscillation time series. The average logarithmic decrement $\delta = \frac{1}{n}\sum_{i=1}^{i=n} \ln \frac{|\alpha|_i}{|\alpha|_{i+1}}$ is calculated for each trial, where $|\alpha|_i$ and $|\alpha|_{i+1}$ is the ith and $(i+1)$th peak of the absolute value of the temporal axis ratio $|\alpha|$. The logarithmic decrement is used as a rudimentary detection of any decay of oscillation [93–95]. Nearly all trials retrieve $\delta \approx 0$, an indication of little to no decay with $\approx$50% $\delta < 0$, as shown in Fig. 15(d). We conclude that the oscillations reported in this work are representative of "steady-state" drop dynamics under continuous levitation. Precise quantification of drop orientation during oscillation has remained challenging due to the inherently three-dimensional motion and optical distortions that occur during levitation [9,44,67,96]. Attempts to reconstruct

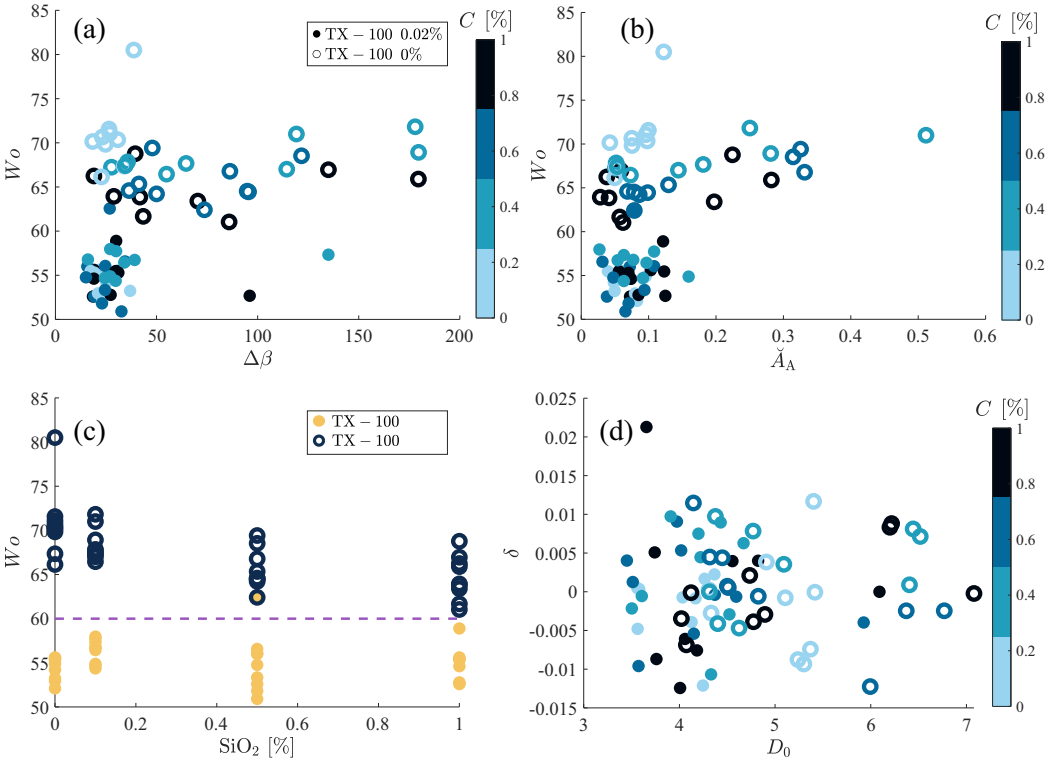

FIG. 15. Womersley number plotted against (a) canting angle amplitude $\Delta\beta$, (b) nondimensionalized axisymmetric amplitude $\check{A}$, and (c) concentration of nanoparticles. (d) Logarithmic decrement δ vs characteristic drop diameter D_0.

the 3D drop shape from 2DVD data are present in the literature [9,45]. Thurai *et al*. [45] use a four-point curvilinear spline interpolation to construct the surface between the two camera planes, an approach that inherently constrains the drop to be approximately oriented orthogonally to the viewing cameras. Zheng *et al*. [9] reconstruct 3D orientation using an oblate spheroidal assumption from field 2DVD observations, reporting statistical distributions of azimuthal and zenith angles. Similarly, canting angle distributions have been inferred from 2DVD drop passages [97]. However, these approaches yield ensemble statistics from transient drop passages rather than time-resolved orientation dynamics of individual drops. To our knowledge, no prior work has tracked the instantaneous 3D orientation of a levitating drop through time, which is the aim of our study. Here, we present an approach that reconstructs the instantaneous three-dimensional orientation of a levitated drop from two orthogonal high-speed camera views. Our method enables a direct measurement of both the azimuthal and zenithal components of the drop oscillatory axis, parameters that have traditionally been inferred indirectly or assumed symmetric [67,71,97].

From our two orthogonal views, as shown in Fig. 16(a), we reconstruct the orientation of the drop as the azimuthal θ and zenith γ angles. The azimuthal is defined as the angle of the drop oscillatory axis as viewed from the top of the observation chamber. The zenith is defined as the angle of incidence of the oscillatory axis from a plane orthogonal to the viewing planes.

The axis ratio α seen in each camera oscillates at similar frequencies, resulting in sinusoidal values that come in and out of phase with one another, as shown in Fig. 16(b). The phase difference between the oscillations of the axis ratios of the two cameras is taken as the azimuthal with a mapping of $[0^\circ - 180^\circ \rightarrow 45^\circ - 0^\circ]$. Hilbert transformations of the two responses of the axis ratios

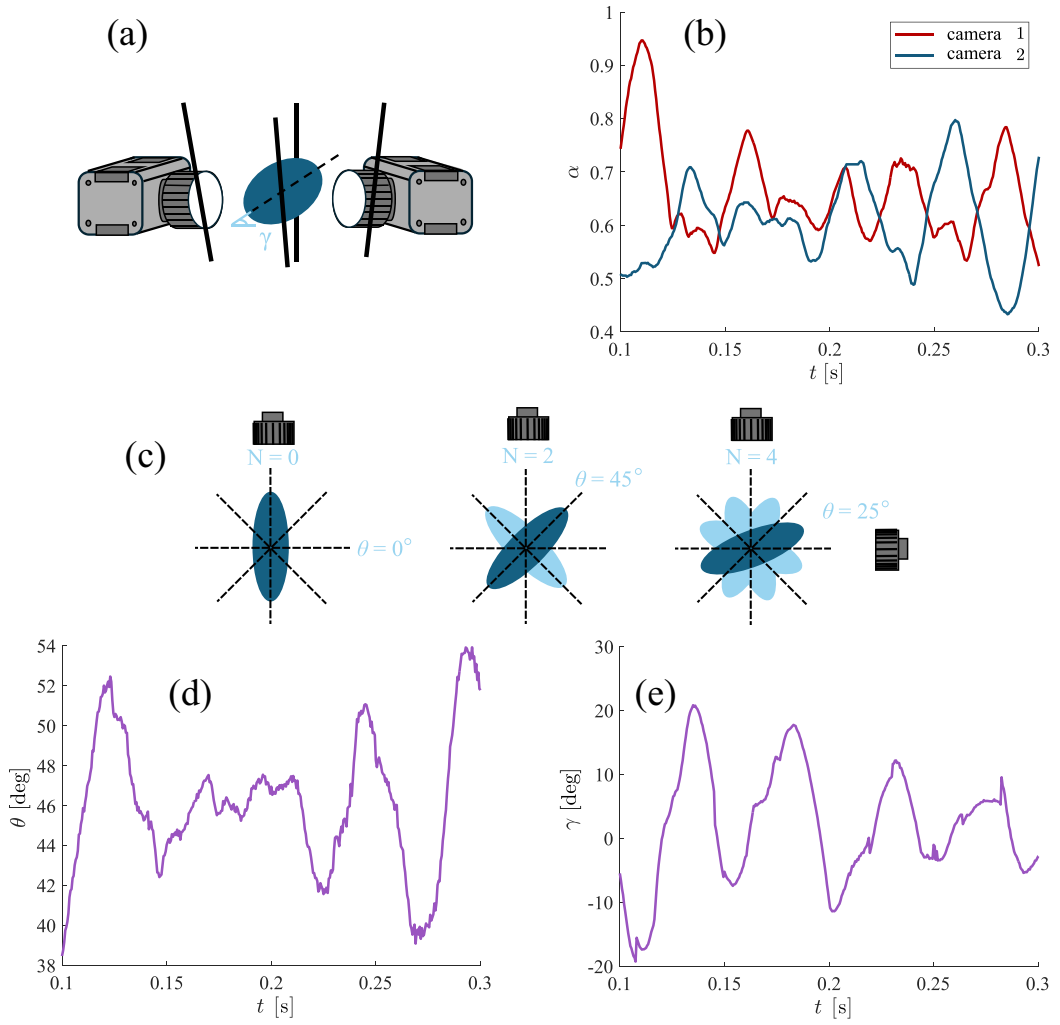

FIG. 16. (a) Schematic of the zenith angle γ of the drop within our two-camera experimental setup. (b) Axis ratio α plotted against time t for both camera views. (c) Illustration of degeneracies $N = 0$, $N = 2$, and $N = 4$ for θ. (d) Zenith angle γ plotted against time. (e) Azimuthal angle θ plotted against time.

are performed to retrieve the complex form of the discrete function. The phase angles are then extracted and the difference is shifted by adding multiples of $\pm 2\pi$ to obtain $|\theta_r| < \pi$, where θ_r is the phase between the axis ratios in radians. θ_r is mapped as $\theta = |180^\circ - 180(\theta_r)/\pi|/4$, where θ is the azimuthal in degrees. There exist degeneracies along different orientations, as shown in Fig. 16(c), which depicts top views of the drop at various θ. At $\theta = 0^\circ$, there exist $N = 0$ degeneracies as the oscillatory axis is completely orthogonal to the viewing planes. At $\theta = 45^\circ$, there exist $N = 2$ degeneracies. All other values have $N = 4$ degeneracies.

The azimuthal and zenith angles change through time, as shown in Figs. 16(c) and 16(d). The zenith angle is taken to be the average canting angle from both cameras, except when $\theta \to 0^\circ$. When $\theta \approx 0^\circ$, the camera that has the shorter horizontal axis loses any information on β so that γ is taken as the maximum of the two canting angles.

Large drops (>6 mm) exhibit unique oscillation patterns with greater amplitudes and lower frequencies. A comparison of small drops (<6 mm) to large drops is shown in Fig. 17. Drops that

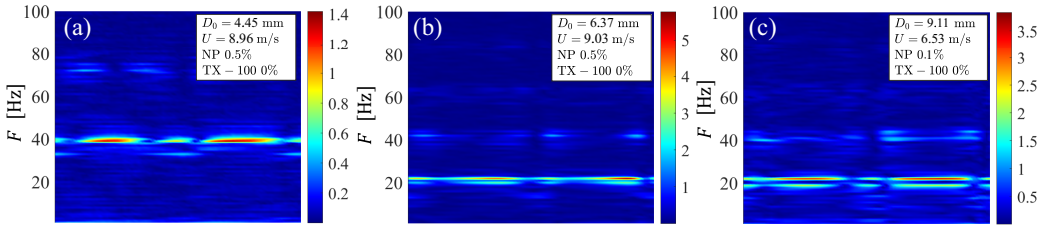

FIG. 17. (a) Spectrogram of small drop with $C = 0.5\%$. (b) Spectrogram of typical large drop with $C = 0.5\%$. (c) Spectrogram of large drop with $C = 0.5\%$ containing multiple frequencies of the same oscillation mode.

are <6 mm tend to have higher frequencies and display defined oscillation modes. The 4.45 mm drop in Fig. 17(a) displays the main pronounced axisymmetric oscillation mode, and the beating pattern beyond 80 Hz indicates the higher-order $n = 3$ oscillation. The main frequency band in the 6.37 mm drop displayed in Fig. 17(b) does not have definite intensities at $\pi n/2$ radians and instead shows similarities with the transverse oscillation mode. We observe that certain large drops contain the same oscillation mode at different frequencies. The Rayleigh theory of oscillation assumes a spherical shape with minimal distortion [87]. Such a shape hosts degenerate oscillation modes along each harmonic. As raindrops >1 mm naturally begin to flatten and oblate, the individual oscillation modes in the dominant $n = 2$ harmonic deviate from the degeneracies [5,43,90]. Our large (> 6 mm) drops contain significant oblation, and drops of this size are found to be near breakup conditions [70,91,92], often oscillating about a flattened equilibrium shape. The high deformation near breakup conditions is enough to significantly deviate from the Rayleigh model and produce the appearance of multiple oscillation modes that we observe. An example can be seen in the 9.11 mm drop in Fig. 17(c), which contains two frequency peaks near 20 Hz for the axisymmetric oscillation mode.

IV. CONCLUSION

In this work, we introduce different methods to characterize drop oscillation and shape. We use a two-camera setup inspired by two-dimensional video disdrometers which are widely used to study rain rate and drop size during precipitation events [67]. The close proximity of our cameras to the site of the drop observation allows for negligible distortion and 3D reconstruction of drop orientation. The prevailing drop shadow in each camera view throughout the oscillation of the drop in time is extracted as the characteristic shape. A volume-equivalent characteristic diameter D_0 is retrieved from the disk integration of the characteristic shape. We find good agreement of D_0 with models of axis ratio and the characteristic shape with the equilibrium drop shape [76]. Frequency analysis along the drop shadow perimeter visualizes all oscillation modes and allows for analysis of drop oscillation amplitude. The three most prominent oscillation modes are axisymmetric, horizontal, and the higher-order ($n = 3$) harmonic, which occur in nearly all our levitated drops. The axisymmetric oscillation mode is the most prominent; its measured frequency and amplitude are the most resilient to noise and errors. The nondimensionalized total oscillation amplitude $\breve{A}$ is a single quantity that can be used to compare the degree of oscillation between levitating drops. The addition of surfactant shifts the NSC to a greater concentration. We suspect that this is due to our surfactant (1.45 CMC) forming micelles and capturing particles from the fluid interface [35], thus decreasing the saturation at the fluid surface. We show that the drag coefficient of raindrops is linear with Reynolds number and approaches the C_d of a solid sphere as the drop size decreases to a critical value. Our work is an experimental validation of all the accumulated theoretical work on raindrop studies since 1879. Future works can investigate the internal circulation within the levitating drops.

ACKNOWLEDGMENTS

This research was done at the Fluids and Structures Laboratory and funded by the National Science Foundation (NSF GEO Grant No. 2201828). We thank Jacob Dockery for late-stage experimental efforts towards the levitation of small drops. We thank Dr. Andy Sarles and McKayla Torbett for goniometer access.

DATA AVAILABILITY

The data that support the findings of this article are openly available [98]; embargo periods may apply.

[1] B. J. Finlayson-Pitts and J. N. Pitts Jr, *Chemistry of the Upper and Lower Atmosphere: Theory, Experiments, and Applications* (Elsevier, Amsterdam, 1999).

[2] K. Sudheer, J. Thomas, P. Jainet, S. Nizar, S. Beegum, D. E. Sebastian, Jesna, and D. Pai, Chapter 8—From science to policy—Toward an approach linking extreme rainfall events to climate resilience and policy development: A case study from Kerala, India, in *Modeling and Mitigation Measures for Managing Extreme Hydrometeorological Events Under a Warming Climate*, edited by K. Kasiviswanathan, B. Soundharajan, S. Patidar, J. He, and C. S. P. Ojha (Elsevier, Amsterdam, 2023), Vol. 14, pp. 143.

[3] P. K. Wang, Theoretical studies on the motions of cloud and precipitation particles—A review, Meteorology **1**, 288 (2022).

[4] T. Schumann, B. Zinder, and A. Waldvogel, Aerosol and hydrometeor concentrations and their chemical composition during winter precipitation along a mountain slope—I. Temporal evolution of the aerosol, microphysical and meteorological conditions, Atmos. Environ. (1967) **22**, 1443 (1988).

[5] M. Szakáll, S. K. Mitra, K. Diehl, and S. Borrmann, Shapes and oscillations of falling raindrops—A review, Atmos. Res. **97**, 416 (2010).

[6] S. Müller, M. Szakáll, S. K. Mitra, K. Diehl, and S. Borrmann, Shapes and oscillations of raindrops with reduced surface tensions: Measurements at the Mainz vertical wind tunnel, Atmos. Res. **119**, 38 (2013).

[7] T. Mega, M. K. Yamamoto, M. Abo, Y. Shibata, H. Hashiguchi, N. Nishi, T. Shimomai, Y. Shibagaki, M. Yamamoto, V. N. Yamanaka, *et al.*, First simultaneous measurement of vertical air velocity, particle fall velocity, and hydrometeor sphericity in stratiform precipitation: Results from 47 MHz wind-profiling radar and 532 nm polarization lidar observations, Radio Sci. **47**, RS3002 (2012).

[8] V. N. Bringi, V. Chandrasekar, J. Hubbert, E. Gorgucci, W. L. Randeu, and M. Schoenhuber, Raindrop size distribution in different climatic regimes from disdrometer and dual-polarized radar analysis, J. Atmos. Sci. **60**, 354 (2003).

[9] H. Zheng, Y. Zhang, H. Li, Z. Wu, and Z. Zhou, Revisiting raindrop axis ratios based on 3D oblate spheroidal reconstruction: 2D video disdrometer observations during tropical cyclone passages, Geophys. Res. Lett. **50**, e2023GL103281 (2023).

[10] D. Rosenfeld and I. M. Lensky, Satellite-based insights into precipitation formation processes in continental and maritime convective clouds, Bull. Am. Meteorol. Soc. **79**, 2457 (1998).

[11] X. Zhang, M. Wang, S. Guo, Z. Zhang, and H. Li, Effects of weathering and rainfall conditions on the release of SiO_2, Ag, and TiO_2 engineered nanoparticles from paints, J. Nanopart. Res. **19**, 338 (2017).

[12] H. R. Pruppacher and K. V. Beard, A wind tunnel investigation of the internal circulation and shape of water drops falling at terminal velocity in air, Q. J. R. Meteorol. Soc. **96**, 247 (1970).

[13] K. V. Beard, V. Bringi, and M. Thurai, A new understanding of raindrop shape, Atmos. Res. **97**, 396 (2010).

[14] B. R. Konan, V. Yoboue, B. Adiaffi, M. Diaby, Y. M. S. Oga, A. Bakayoko, S. Gnamien, S. Keita, J. Bahino, and M. Ossohou, Source of polycyclic aromatic hydrocarbons (PAHs) in rainwater and effect on

the health of the population: The case of the district of Abidjan in the south of Ivory Coast, J. Water and Health **20**, 985 (2022).
[15] J. Rosinski and T. C. Kerrigan, The role of aerosol particles in the formation of raindrops and hailstones in severe thunderstorms, J. Atmos. Sci. **26**, 695 (1969).
[16] B. J. Green, M. Dettmann, E. Yli-Panula, S. Rutherford, and R. Simpson, Atmospheric Poaceae pollen frequencies and associations with meteorological parameters in Brisbane, Australia: A 5-year record, 1994–1999, Int. J. Biometeorol. **48**, 172 (2004).
[17] A. C. Jones, A. Hill, J. Hemmings, P. Lemaitre, A. Quérel, C. L. Ryder, and S. Woodward, Below-cloud scavenging of aerosol by rain: A review of numerical modelling approaches and sensitivity simulations with mineral dust in the Met Office's Unified Model, Atmos. Chem. Phys. **22**, 11381 (2022).
[18] J. Fan, D. Rosenfeld, Y. Zhang, S. E. Giangrande, Z. Li, L. A. T. Machado, S. T. Martin, Y. Yang, J. Wang, P. Artaxo, *et al.*, Substantial convection and precipitation enhancements by ultrafine aerosol particles, Science **359**, 411 (2018).
[19] C. Anastasio and S. T. Martin, Atmospheric nanoparticles, Rev. Mineral. Geochem. **44**, 293 (2001).
[20] G. Cherrier, E. Belut, F. Gerardin, A. Tanière, and N. Rimbert, Aerosol particles scavenging by a droplet: Microphysical modeling in the Greenfield gap, Atmos. Environ. **166**, 519 (2017).
[21] C. Blanco-Alegre, A. Castro, A. I. Calvo, F. Oduber, E. Alonso-Blanco, D. Fernández-González, R. M. Valencia-Barrera, A. M. Vega-Maray, and R. Fraile, Below-cloud scavenging of fine and coarse aerosol particles by rain: The role of raindrop size, Q. J. R. Meteorol. Soc. **144**, 2715 (2018).
[22] W. Jung, H. M. Sung, C.-H. You, H.-J. Kim, S.-H. Suh, D.-I. Lee, and K.-H. Chang, Relationships between aerosol and raindrop size distributions during rainfall period (Changma) in Jeju Island, Korea, Atmosphere **13**, 933 (2022).
[23] C. Andronache, Estimated variability of below-cloud aerosol removal by rainfall for observed aerosol size distributions, Atmos. Chem. Phys. **3**, 131 (2003).
[24] J. F. Sisler and W. C. Malm, The relative importance of soluble aerosols to spatial and seasonal trends of impaired visibility in the United States, Atmos. Environ. **28**, 851 (1994).
[25] P. J. DeMott, D. C. Rogers, and S. M. Kreidenweis, The susceptibility of ice formation in upper tropospheric clouds to insoluble aerosol components, J. Geophys. Res.: Atmos. **102**, 19575 (1997).
[26] H. R. Pruppacher and J. D. Klett, *Microphysics of Clouds and Precipitation, Atmospheric and Oceanographic Sciences Library*, 2nd ed. (Springer, Dordrecht, Netherlands, 1996).
[27] P. Jungwirth and D. J. Tobias, Specific ion effects at the air/water interface, Chem. Rev. **106**, 1259 (2006).
[28] B. R. Bzdek, A. J. Horan, M. R. Pennington, N. J. Janechek, J. Baek, C. O. Stanier, and M. V. Johnston, Silicon is a frequent component of atmospheric nanoparticles, Environ. Sci. Technol. **48**, 11137 (2014).
[29] C. Zhang, L. Bu, F. Fan, N. Ma, Y. Wang, Y. Yang, J. Größ, J. Yan, and A. Wiedensohler, Surfactant effect on the hygroscopicity of aerosol particles at relative humidity ranging from 80 adipic acid-ammonium sulfate particles, Atmos. Environ. **266**, 118725 (2021).
[30] D. A. Sodeman, S. M. Toner, and K. A. Prather, Determination of single particle mass spectral signatures from light-duty vehicle emissions, Environ. Sci. Technol. **39**, 4569 (2005).
[31] L. K. Koopal, T. P. Goloub, and T. A. Davis, Binding of ionic surfactants to purified humic acid, J. Colloid Interface Sci. **275**, 360 (2004).
[32] A. Milsom, A. M. Squires, A. D. Ward, and C. Pfrang, Molecular self-organization in surfactant atmospheric aerosol proxies, Acc. Chem. Res. **56**, 2555 (2023).
[33] R. J. Ambrose, Surfactants and interfacial phenomena—Second edition, by Milton J. Rosen, John Wiley and Sons, Inc., New York, (1989), 431pp. price: $49.95, J. Polymer Sci. Part C: Polymer Lett. **27**, 503 (1989).
[34] H. Manikantan and T. M. Squires, Surfactant dynamics: Hidden variables controlling fluid flows, J. Fluid Mech. **892**, P1 (2020).

[35] H. Jia, W. Huang, Y. Han, Q. Wang, S. Wang, J. Dai, Z. Tian, D. Wang, H. Yan, and K. Lv, Systematic investigation on the interaction between SiO_2 nanoparticles with different surface affinity and various surfactants, J. Mol. Liq. **304**, 112777 (2020).
[36] S. E. Hinkle, A modified empirical drag coefficient for water drop ballistics, Appl. Eng. Agric. **7**, 75 (1991).
[37] R. Gunn and G. D. Kinzer, The terminal velocity of fall for water droplets in stagnant air, J. Atmos. Sci. **6**, 243 (1949).
[38] H. Kaur, A. Sobti, R. K. Wanchoo, and A. P. Toor, Experimental study on hydrodynamic behaviour of nanofluid particle moving through an immiscible quiescent liquid, Results Eng. **16**, 100760 (2022).
[39] M. Szakáll and I. Urbich, Wind tunnel study on the size distribution of droplets after collision induced breakup of levitating water drops, Atmos. Res. **213**, 51 (2018).
[40] T. E. Hoffer and S. C. Mallen, A vertical wind tunnel for small droplet studies, J. Appl. Meteor. **7**, 290 (1968).
[41] R. D. Lorenz, Raindrops on Titan, Adv. Space Res. **15**, 317 (1995).
[42] M. L. Yakubu, Z. Yusop, and, M. L. Fulazzaky, The influence of rain intensity on raindrop diameter and the kinetics of tropical rainfall: Case study of Skudai, Malaysia, Hydrol. Sci. J. **61**, 944 (2016).
[43] Beard and R. J. Kubesh, Laboratory measurements of small raindrop distortion. Part 2: Oscillation frequencies and modes, J. Atmos. Sci. **48**, 2245 (1991).
[44] M. Szakáll, K. Diehl, S. K. Mitra, and S. Borrmann, A wind tunnel study on the shape, oscillation, and internal circulation of large raindrops with sizes between 2.5 and 7.5 mm, J. Atmos. Sci. **66**, 755 (2009).
[45] M. Thurai, V. N. Bringi, A. B. Manić, N. J. Šekeljić, and B. M. Notaroš, Investigating raindrop shapes, oscillation modes, and implications for radio wave propagation, Radio Sci. **49**, 921 (2014).
[46] M. Zhang, J. Yang, Z. Cai, Y. Feng, Y. Wang, D. Zhang, and X. Pan, Detection of engineered nanoparticles in aquatic environments: Current status and challenges in enrichment, separation, and analysis, Environ. Sci.: Nano **6**, 709 (2019).
[47] N. B. Portela, E. C. Teixeira, D. M. Agudelo-Castañeda, M. da Silva Civeira, L. F. O. Silva, A. Vigo, and P. Kumar, Indoor-outdoor relationships of airborne nanoparticles, BC and VOCs at rural and urban preschools, Environ. Pollut. **268**, 115751 (2021).
[48] M. Dia, P.-E. Peyneau, D. Courtier-Murias, and B. Bechet, Detection and quantification of nanoparticles in runoff from a highly trafficked urban motorway, Environ. Sci.: Nano (2025).
[49] S. Smita, S. K. Gupta, A. Bartonova, M. Dusinska, A. C. Gutleb, and Q. Rahman, Nanoparticles in the environment: Assessment using the causal diagram approach, Environ. Health **11**, S13 (2012).
[50] K. Michel, J. Scheel, S. Karsten, N. Stelter, and T. Wind, Risk assessment of amorphous silicon dioxide nanoparticles in a glass cleaner formulation, Nanotoxicology **7**, 974 (2012).
[51] Federal Register :: Request Access—ecfr.gov, https://www.ecfr.gov/current/title-21/chapter-I/subchapter-E/part-573/subpart-B/section-573.940, [Accessed 12-04-2025].
[52] L. H. Hai, The effect of SiO_2 nanoparticles in polyurethane paint formulation on metal surfaces, Int. J. Sci. Res. Arch. **3**, 031 (2021).
[53] G. Yalçın, S. Öztuna, A. S. Dalkılıç, and S. Wongwises, Effect of particle size on SiO_2 nanofluid viscosity determined by a two-step method, J. Therm. Anal. Calorim. **149**, 13681 (2024).
[54] M. Rejvani, A. Alipour, S. M. Vahedi, A. J. Chamkha, and S. Wongwises, Optimal characteristics and heat transfer efficiency of SiO_2/water nanofluid for application of energy devices: A comprehensive study, Int. J. Energy Res. **43**, 8548 (2019).
[55] M. Wondie, Modeling cloud seeding technology for rain enhancement over the arid and semiarid areas of Ethiopia, Heliyon **9**, e14974 (2023).
[56] G. Mehdizadeh, E. Erfani, F. McDonough, and F. Hosseinpour, Quantifying the influence of cloud seeding on ice particle growth and snowfall through idealized microphysical modeling, Atmosphere **15**, 1460 (2024).
[57] F. Hoffmann and G. Feingold, Cloud microphysical implications for marine cloud brightening: The importance of the seeded particle size distribution, J. Atmos. Sci. **78**, 3247 (2021).

[58] F. Renggono, M. Kudsy, K. Adhitya, P. Purwadi, H. A. Belgaman, S. Dewi, R. Syahdiza, E. Mulyana, E. Aldrian, and J. Arifian, Hygroscopic ground-based generator cloud seeding design; a case study from the 2020 weather modification in Larona Basin Indonesia, Atmosphere **13**, 968 (2022).
[59] J. D. Dockery, D. Y. Aydin, and A. K. Dickerson, Pendant drop motion and stability in vertical airflow, Phys. Fluids **36**, 027107 (2024).
[60] R. D. Mehta and P. Bradshaw, Design rules for small low speed wind tunnels, Aeronaut. J. **83**, 443 (1979).
[61] Dassault Systèmes, 2025, SolidWorks (2025) [Computer software], https://www.solidworks.com.
[62] F. Testik and M. Rahman, High-speed optical disdrometer for rainfall microphysical observations, J. Atmos. Ocean. Technol. **33**, 231 (2016).
[63] H. Ismail, M. Z. Sulaiman, and M. A. H. Aizzat, Qualitative investigations on the stability of Al_2O_3-SiO_2 hybrid water-based nanofluids, IOP Conf. Ser.: Mater. Sci. Eng. **788**, 012091 (2020).
[64] A. H. Milyani, M. A. Al-Ebrahim, E. T. Attar, N. H. Abu-Hamdeh, M. E. Mostafa, O. K. Nusier, A. Karimipour, and B. N. Le, Artificial intelligence optimization and experimental procedure for the effect of silicon dioxide particle size in silicon dioxide/deionized water nanofluid: Preparation, stability measurement and estimate the thermal conductivity of produced mixture, J. Mater. Res. Technol. **26**, 2575 (2023).
[65] P. K. Das, A. K. Santra, R. Ganguly, S. K. Dash, S. Muthusamy, M. Sha, and K. K. Sadasivuni, An extensive review of preparation, stabilization, and application of single and hybrid nanofluids, J. Therm. Anal. Calorim. **149**, 9523 (2024).
[66] D. Ghosh, S. Das, V. K. Gahlot, M. Pulimi, S. Anand, N. Chandrasekaran, P. K. Rai, and A. Mukherjee, A comprehensive estimate of the aggregation and transport of $nSiO_2$ in static and dynamic aqueous systems, Environ. Sci.: Processes Impacts **24**, 675 (2022).
[67] A. Kruger and W. F. Krajewski, Two-dimensional video disdrometer: A description, J. Atmos. Ocean. Technol. **19**, 602 (2002).
[68] J. Yousefi, Image binarization using Otsu thresholding algorithm, Ontario, Canada: University of Guelph **10**, 9 (2011).
[69] See Supplemental Material at http://link.aps.org/supplemental/10.1103/s7rj-swb3 for additional methods on elliptical integration, spectra lacking a distinct horizontal oscillation mode, and concentration- and Reynolds-number trends of individual oscillation amplitudes.
[70] K. V. Beard and C. C. Chuang, A new model for the equilibrium shape of raindrops, J. Atmos. Sci. **44**, 1509 (1987).
[71] K. V. Beard, V. Bringi, and M. Thurai, A new understanding of raindrop shape, Atmos. Res. **97**, 396 (2010).
[72] K. Andsager, K. V. Beard, and N. F. Laird, Laboratory measurements of axis ratios for large raindrops, J. Atmos. Sci. **56**, 2673 (1999).
[73] J. Pan, W. Wang, Y. Wei, J. Chen, and L. Wang, A calculation model of critical liquid-carrying velocity of gas wells considering the influence of droplet shapes, Nat. Gas Ind. B **5**, 337 (2018).
[74] W. R. Goossens, Review of the empirical correlations for the drag coefficient of rigid spheres, Powder Technol. **352**, 350 (2019).
[75] R. Clift and W. H. Gauvin, Motion of entrained particles in gas streams, Can. J. Chem. Eng. **49**, 439 (1971).
[76] K. V. Beard, Terminal velocity and shape of cloud and precipitation drops aloft, J. Atmos. Sci. **33**, 851 (1976).
[77] F. Y. Testik and A. Bolek, Wind and turbulence effects on raindrop fall speed, J. Atmos. Sci. **80**, 1065 (2023).
[78] G. B. Foote and P. S. D. Toit, Terminal velocity of raindrops aloft, J. Appl. Meteor. **8**, 249 (1969).
[79] S. Al-Anssari, S. Wang, A. Barifcani, and S. Iglauer, Oil-water interfacial tensions of silica nanoparticle-surfactant formulations, Tenside Surf. Det. **54**, 334 (2017).
[80] L. Dong and D. T. Johnson, Surface tension of charge-stabilized colloidal suspensions at the water–air interface, Langmuir **19**, 10205 (2003).
[81] S. Fusco, L. Liu, M. Á. Cabrerizo-Vílchez, E. Koos, and M. Á. Rodríguez-Valverde, Vibration-triggered spreading of nanofluid drops, Phys. Fluids **36**, 052014 (2024).

[82] S. Frijters, F. Günther, and J. Harting, Effects of nanoparticles and surfactant on droplets in shear flow, Soft Matter **8**, 6542 (2012).
[83] R. Wang, Nanoparticles influence droplet formation in a T-shaped microfluidic, J. Nanopart. Res. **15**, 2128 (2013).
[84] G. Lu, Y.-Y. Duan, and X.-D. Wang, Surface tension, viscosity, and rheology of water-based nanofluids: A microscopic interpretation on the molecular level, J. Nanopart. Res. **16**, 2564 (2014).
[85] V. Singh and R. Tyagi, Investigations of mixed surfactant systems of lauryl alcohol based bissulfosuccinate anionic gemini surfactant with conventional surfactants: A fluorometric study, J. Taibah Univ. Sci. **9**, 477 (2015).
[86] K. P. Sharma, V. K. Aswal, and G. Kumaraswamy, Adsorption of nonionic surfactant on silica nanoparticles: Structure and resultant interparticle interactions, J. Phys. Chem. B **114**, 10986 (2010).
[87] L. Rayleigh, On the capillary phenomena of jets, Proc. R. Soc. London **29**, 71 (1879).
[88] H. Lamb, *Cambridge Mathematical Library: Hydrodynamics*, 6th ed. (Cambridge University Press, Cambridge, England, 1993).
[89] A. R. Nelson and N. R. Gokhale, Oscillation frequencies of freely suspended water drops, J. Geophys. Res. **77**, 2724 (1972).
[90] J. Q. Feng and K. V. Beard, A perturbation model of raindrop oscillation characteristics with aerodynamic effects, J. Atmos. Sci. **48**, 1856 (1991).
[91] E. Villermaux and B. Bossa, Single-drop fragmentation determines size distribution of raindrops, Nat. Phys. **5**, 697 (2009).
[92] D. C. Blanchard and A. T. Spencer, Experiments on the generation of raindrop-size distributions by drop breakup, J. Atmos. Sci. **27**, 101 (1970).
[93] Fayyaz, S. Bashmal, A. Nazir, S. Khan, and A. Alofi, Damping optimization and energy absorption of mechanical metamaterials for enhanced vibration control applications: A critical review, Polymers **17**, 237 (2025).
[94] D. J. Tweten, Z. Ballard, and B. P. Mann, Minimizing error in the logarithmic decrement method through uncertainty propagation, J. Sound Vib. **333**, 2804 (2014).
[95] Y. Liao and V. Wells, Modal parameter identification using the log decrement method and band-pass filters, J. Sound Vib. **330**, 5014 (2011).
[96] Y. Sasaki, K. Kobayashi, K. Hasegawa, A. Kaneko, and Y. Abe, Transition of flow field of acoustically levitated droplets with evaporation, Phys. Fluids **31**, 102109 (2019).
[97] G.-J. Huang, V. N. Bringi, and M. Thurai, Orientation angle distributions of drops after an 80-m fall using a 2D video disdrometer, J. Atmos. Ocean. Technol. **25**, 1717 (2008).
[98] G. P. S. Rible, Aerodynamic levitation of nanofluid drops, GitHub repository (2026), https://github.com/genepatrickrible/Aerodynamic-levitation-of-nanofluid-drops, https://doi.org/10.5281/zenodo.17488371.